Cosmic ray validation of electrode positions in small-strip thin gap chambers for the upgrade of the ATLAS detector

Lia Formenti

Department of Physics
McGill University, Montreal
October, 2021

A thesis submitted to
McGill University
in partial fulfillment of the
requirements of the degree of
Master of Science

Table of Contents

Abstract

The Large Hadron Collider (LHC) is used to generate subatomic physics processes at the energy frontier to challenge our understanding of the Standard Model of particle physics. The particle collision rate at the LHC will be increased up to seven times its design value in 2025-2027 by an extensive upgrade program. The innermost endcaps of the ATLAS muon spectrometer consist of two wheels of muon detectors that must be replaced to maintain the muon momentum resolution in the high-rate environment. The so-called New Small Wheels (NSWs) are made of two detector technologies: micromegas and small-strip thin gap chambers (sTGCs). The sTGCs are gas ionization chambers that hold a thin volume of gas between two cathode boards. One board is segmented into copper readout strips of 3.2 mm pitch that are used to precisely reconstruct the coordinate of a passing muon. Modules of four sTGCs glued together into quadruplets cover the NSWs. Quadruplets were designed to achieve a 1 mrad angular resolution to fulfill the spectrometer's triggering and precision tracking requirements. To achieve the required angular resolution the absolute position of the readout strips must be known in the ATLAS coordinate system to within 100 µm. At McGill University, the performance of sTGC quadruplets was characterized using cosmic ray data before being sent to CERN, where the charge profile left by x-rays is used to measure the offset of the strip patterns with respect to nominal at a limited number of points on the surface of each quadruplet. The x-ray strip position measurements have acceptable but limited precision and do not span the whole area of the strip layers. Given the importance of knowing the absolute position of each readout strip to achieve the performance requirements of the NSWs, the x-ray method must be validated by an independent method. Cosmic ray data is used to characterize the relative alignment between layers and validate the x-ray method.

Résumé

Le collisioneur LHC est utilisé pour générer des processus de la physique subatomique à la frontière d'énergie pour remettre en cause le modèle standard de la physique des particules. Le taux des collisions du collisioneur LHC augmontera jusqu'à sept fois le taux nominal en 2025-2027 par un programme d'amélioration majeur et varié. Une partie du spectromètre à muons est composée de deux roues de détecteurs de muons qu'il faut remplacer pour mantenir la résolution d'élan après l'augmentation du taux. Appelées les Nouvelles Petites Roues (NSWs), elles en utilisent deux technologies: des chambres micromegas et des chambres sTGCs (chambres à petites bandes et à intervalles fins). Les sTGCs sont des chambres d'ionisation de gaz, qui contiennent un volume de gaz fin entre deux panneaux cathodiques. Un panneau est segmenté à petites bandes en cuivre avec une pente de 3.2 mm qui se servent comme des voies de signal pour reconstruire précisement la coordonnée d'un muon qui passe. Des modules de quatres sTGCs collées ensembles en quaduplets couvrent les NSWs. Les quadruplets étaient conçus pour réaliser une résolution angulaire de 1 mrad pour satisfaire les exigences des systèmes de déclenchement et de mésures de précision. Pour réaliser la résolution angulaire il faut que la position absolue de chaque bande soit connue dans ATLAS avec une précision à moins de 100 µm. À l'Université de McGill, la performance des quadruplets étaient caractériser avec des rayons cosmiques avant les envoyer à CERN, où le profil de charge laisser par des rayons-X est utilisé pour mesurer le déplacement du motif des bandes par rapport à nominal à un nombre de position limité sur la surface des quadruplets. Les déplacements mesurés pas les rayons-X ont une précision acceptable mais limitée, et ne couvrent pas la région entière des panneaux. Étant donné l'importance de savoir la position absolue de chaque bande pour réaliser les exigences de performance des NSWs, il faut une méthode indépendente pour valider la méthode des rayons-X. Les données recuellies avec les rayons cosmiques sont utilisées pour charactariser l'alignement relatif entre les panneaux et pour valider la méthode des rayons-X.

Acknowledgements

Experimental particle physics projects are never done alone. I am grateful to have been working with the ATLAS Collaboration for two years now.

Thank you to Dr. Brigitte Vachon for her guidance throughout this project and for editing this thesis. I am consistently amazed by her ability to jump into the details of my project and discuss them with me.

Thanks also to Dr. Benoit Lefebvre, who collected some of the data used in this thesis, wrote several software tools I used to analyze the data and advised me several times throughout this project.

Thank you to my labmates at McGill University, Dr. Tony Kwan, Kathrin Brunner, John McGowan and Charlie Chen. Kathrin taught me mechanical skills that I will apply elsewhere. Tony, manager of the laboratory, created the most encouraging, trusting and productive work environment I have ever been apart of.

Thank you to the friends I can call on at anytime, and thank you to my family whose constant support makes every step possible.

Contribution of authors

I, the author, was involved in collecting the cosmic ray data from September 2019 - March 2021. I did not design the cosmic ray testing procedure nor write the data preparation software, but I participated in using the software to analyze cosmic ray results. In the thesis, the terms "clustering," "local offset" and "relative local offset" are defined. Cosmic ray clustering was done in the data preparation software, but I redid the fit afterwards to explore sensitivity to the fit algorithm. With help from Dr. Lefebvre and Dr. Vachon, I helped design the software that calculated the relative local offsets from cosmic ray data. I wrote that software on my own. I was not involved in the design, data collection, data preparation or analysis of the x-ray data. I also was not involved in creating an alignment model from the x-ray data. I used the x-ray local offsets calculated using x-ray data analysis software to calculate relative local offsets with x-rays. I did the comparison between the x-ray and cosmic ray data.

I hereby declare that I am the sole author of this thesis. This is a true copy of the thesis, including any required final revisions, as accepted by my examiners.

Chapter 1

Introduction

The Standard Model (SM) is a theoretical framework that describes experimental observations of particles and their interactions at the smallest distance scales; however, the questions the SM does not address motivate more experimentation.

Accelerators collide particles to generate interactions that can be recorded by detectors for further study. Detectors measure the trajectory and energy of all secondary particles produced in collisions to understand the interaction. The Large Hadron Collider (LHC) [1] at CERN is the world's most energetic particle accelerator. Its energy makes it a unique tool to study elementary particles and their interactions in an environment with conditions similar to what would have existed in the early universe. If study at the energy frontier is to continue, the LHC must go on.

After 2025, the statistical gain in running the LHC further without significant increase in beam intensity will become marginal. The High Luminosity Large Hadron Collider (HL-LHC) project [2] is a series of upgrades to LHC infrastructure that will allow the LHC to collect approximately ten times more data than in the initial design by $\sim$2030. The increase in LHC beam intensity will result in a large increase in collision rate that will make accessible and improve statistics on several measurements of interest [3], many only possible at the LHC and the energy frontier. The increase in beam intensity will also increase the level of background radiation, requiring major upgrades to the experiments used to record the outcomes of the particle collisions.

The ATLAS experiment [4] is one of the LHC's general-purpose particle detector arrays, positioned around one of the collision points of the LHC. During the 2019-2022 Long Shutdown of the LHC, the most complex upgrade of the ATLAS experiment is the replacement of the small wheels of the muon spectrometer with the so-called New Small Wheels (NSWs) [5].

The detector upgrade addresses both the expected decrease in hit efficiency of the precision tracking detectors and the high fake trigger rate expected in the muon spectrometer at the HL-LHC. The NSWs are made of two different detector technologies: micromegas and small-strip thin gap chambers (sTGCs). Micromegas are optimized for precision tracking while sTGCs are optimized for rapid triggering, although each will provide complete coverage and measurement redundancy over the area of the NSWs. Eight layers each of sTGCs cover the NSWs. Practically, countries involved in detector constructor created quadruplet modules of four sTGCs glued together that were arranged and installed over the area of the NSWs once they arrived at CERN. Teams across three Canadian institutions built and characterized 1/4 of all the required sTGCs.

The sTGCs are gas ionization chambers that consist of a thin volume of gas held between two cathode boards. One board is segmented into strip readout electrodes of 3.2 mm pitch. The position of the particle track in the precision coordinate can be reconstructed from the strip signals [5]. The sTGCs acheived the design track spatial resolution in the precision coordinate of less than 100 µm per detector plane that will allow them to achieve a 1 mrad track angular resolution using the 8 layers of sTGC on the NSW [6, 5]. The NSW measurement of the muon track angle will be provided to the ATLAS trigger and used to reject tracks that do not originate from the interaction point [5].

The precise measurement of a muon track angle depends on knowing the position of each readout strip within the ATLAS coordinate system. To achieve this, the position of specific locations on the surface of sTGC quadruplets will be monitored by the ATLAS alignment system to account for time-dependent deformations [5]. Within a quadruplet module, the strip positions could have been shifted off of nominal by non-conformities of the strip pattern etched onto each cathode boards [7] and shifts between strip layers while gluing sTGCs into quadruplets.

An xray gun was used to measure the offset of strips from their nominal position at the locations that will be monitored by the ATLAS alignment system thereby providing, locally, an absolute "as-built" strip position within the ATLAS coordinate system. Estimates of the "as-built" positions of every readout strip are obtained by building an alignment model from the available x-ray measurements [8].

The technique of measuring the "as-built" strip positions using xray data has never been used before and must be validated. This thesis describes the use of cosmic muon data, recorded to characterize the performance of each Canadian-made sTGC module, to validate the x-ray strip position measurements. A description of how this work fits within the overall alignment scheme of the NSW is also presented.

Rewrite after implementing Brigitte's edits. Chapters 3 and 4 give more background on particle physics, the LHC, ATLAS, the NSWs, and sTGCs. In chapter 5, the cosmic ray testing procedure and how the position of the strips can be probed with cosmics data is presented. Chapter 6 introduces the x-ray method, and in chapter 7, the x-ray offsets are validated with cosmic muon data. The thesis concludes with a summary and outlook in chapter 8.

Chapter 2

High energy particle physics

Particle physics aims to study the elementary constituents of matter. Understanding the fundamental building blocks and how they interact provides insights into the evolution of the early universe to the forms of matter we observe today. This chapter introduces general concepts in particle physics relevant to understanding the physics goals of the HL-LHC and NSW upgrade.

The information on particle physics and the SM presented here is rather general; the reader is referred to [9, 10, 11] for more information.

2.1 The Standard Model

The Standard Model (SM) is the theoretical framework developed in the early 1970's to describe the observed elementary particles and their interactions. It is built on a collection of quantum field theories and has been remarkably successful at predicting experimental observations, including but not limited to, the existence of the top quark [12], the tau neutrino [13] and the Higgs boson [14, 15].

The known elementary particles described by the SM are represented in figure 2.1. There are 12 matter particles (six quarks and six leptons), 4 force-mediating particles, and the Higgs boson. Each matter particle also has an anti-matter particle pair with the same mass but opposite charge, not represented in figure 2.1. The different forces of nature are understood to be the result of the exchange of force-mediating particles between interacting (coupled) particles. Photons are mediators of the electromagnetic force, W+/- and Z bosons are mediators of the weak force, and gluons are mediators of the strong force. At high

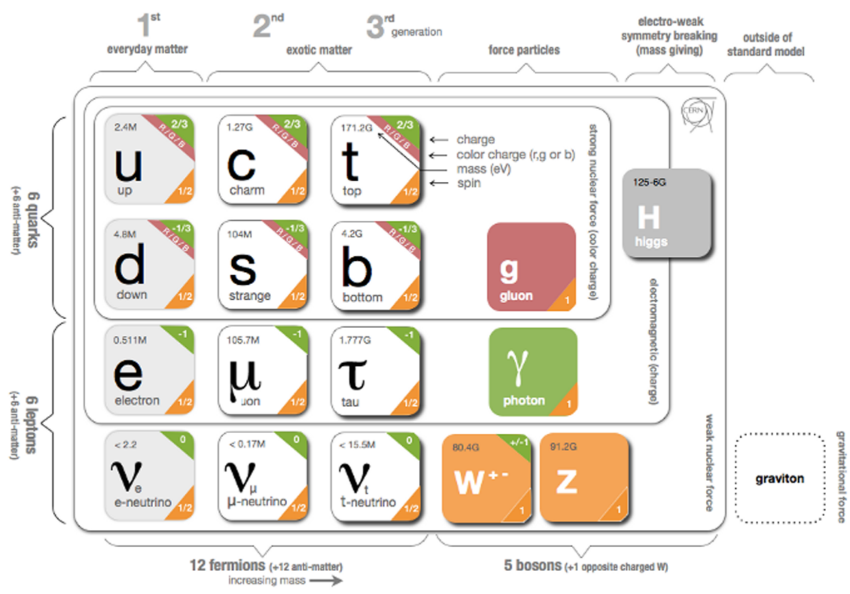

Figure 2.1: Schematic diagram of all elementary particles in the SM. Particles are grouped according to their properties and the forces through which they interact with other particles [16].

energy, the SM describes the electromagnetic and weak forces as stemming from a unified electroweak force.. The Higgs boson field interacts with the particles mediating the unified electroweak force to distinguish the weak and electromagnetic forces from each other at lower energies and give particles (except neutrinos) a mass. This is called electroweak symmetry breaking.

Quarks are matter particles that are sensitive to all forces; notably they are the only particles sensitive to the strong force. Protons and neutrons are made up of quarks and gluons, and the strong force is responsible for their existence and mutual attraction into nuclei [17]. Leptons are particles not sensitive to the strong force. Charged leptons include the electron, which once part of atoms is responsible for chemistry. Of particular importance for this thesis is the charged lepton called a muon. It is like the electron but its mass is ∼200 times larger that that of the electron. Muons have a lifetime of 2.2 µs [11] and decay predominantly as $\mu \to e^- \overline{\nu_e} \nu_\mu$ .Neutrinos are neutral, almost massless leptons that only interact through the weak force.

Common matter is made up of the lightest constituents of the SM: up and down quarks, electrons and photons. The other particles are produced in high-energy environments but then decay to the lightest constituents. Such high energy environments include the conditions present in the early universe [18], astrophysical sources, and particle accelerators. The presence of the particles of the SM at the beginning of the Universe means that their interactions and decays are fundamental for the study of the evolution of the early universe [18]. Many high energy astrophysical sources, like supernovae, generate particles that rain down on Earth as cosmic rays [19]. Particle accelerators have been built to create controlled environments of high-rate particle collisions at high energy where the production and decay of elementary particles can be directly studied..

2.2 Beyond the Standard Model

Despite its success at describing most experimental observations to date, there is ample evidence that the SM is not a complete description of natural phenomena at the smallest scales. For example, the SM has a large number of free parameters, the values of which have to be fine-tuned to fit experimental observations. This is part of the so-called "naturalness" problem.

Furthermore, the SM provides no explanation for several open questions in particle physics. First, neutrinos in the SM are assumed to be massless and do not gain mass in the same way as the other particles. However, in 2013 neutrino were confirmed to change between their different flavours [20], which can only occur if neutrinos do have mass [21]. The neutrino mass requires physics beyond the standard model [22]. Second, several astrophysical and cosmological measurements suggest the presence of “dark matter” making up 85 % of the matter content of the universe [23]. The nature of dark matter is unknown and so far there is no SM explanation [24]. Third, the SM does not explain the origin and nature of the matter-antimatter asymmetry that produced our matter-dominated universe.Finally, the SM does not include a description of gravity.

Theoretical extensions beyond the Standard Model (BSM) aim to address some of these questions, often predicting existence of yet-unseen elementary particles and/or physics phenomena beyond those predicted by the SM. For example, super-symmetry (SUSY) predicts that each SM particle has a heavier super-symmetric partner. SUSY would explain the origin of dark matter with weakly interacting massive particles, would solve the so-called “naturalness” problem in the SM [25]. These hypothetical new physics phenomena and/or new particles can be searched for at particle accelerators.

2.3 Studying high energy particle physics with accelerators

In particular, particle accelerators of increasingly higher energy have a long history of enabling the discovery of predicted, yet-unseen particles. These include, for example, the discovery of the W [26, 27] and Z bosons [28, 29], the top quark [30, 31], and most recently, the discovery of the Higgs boson [32, 33] marking the completion of the SM as it is known today.

Based on the established success of the SM, there are two approaches to particle physics research. One approach is to search for the existence of new physics phenomena predicted to exist in BSM theories and the other is to test the validity of the SM to a high degree of accuracy to search for flaws in the model. Standard Model predictions are generally expressed in terms of the probability of a specific physics process to occur, expressed as a cross section in units of barns (with 1 barn = 10^{-28} m^2). As an example, figure 2.1 shows a summary of cross section measured for different physics processes using the ATLAS experiment and their comparison with the predictions of the SM. Most cross section measurements agree well within one standard deviation with the SM predictions.

Particle accelerators provide a controlled and high-collision rate environment that makes them ideal places to search for new physics phenomena and to carry out systematic tests of the SM. The LHC is the highest energy collider in the world so it can access physics that no other accelerator can, notably the direct production of the Higgs boson and top quark. A description of the LHC and the ATLAS detector are provided in the next chapter.

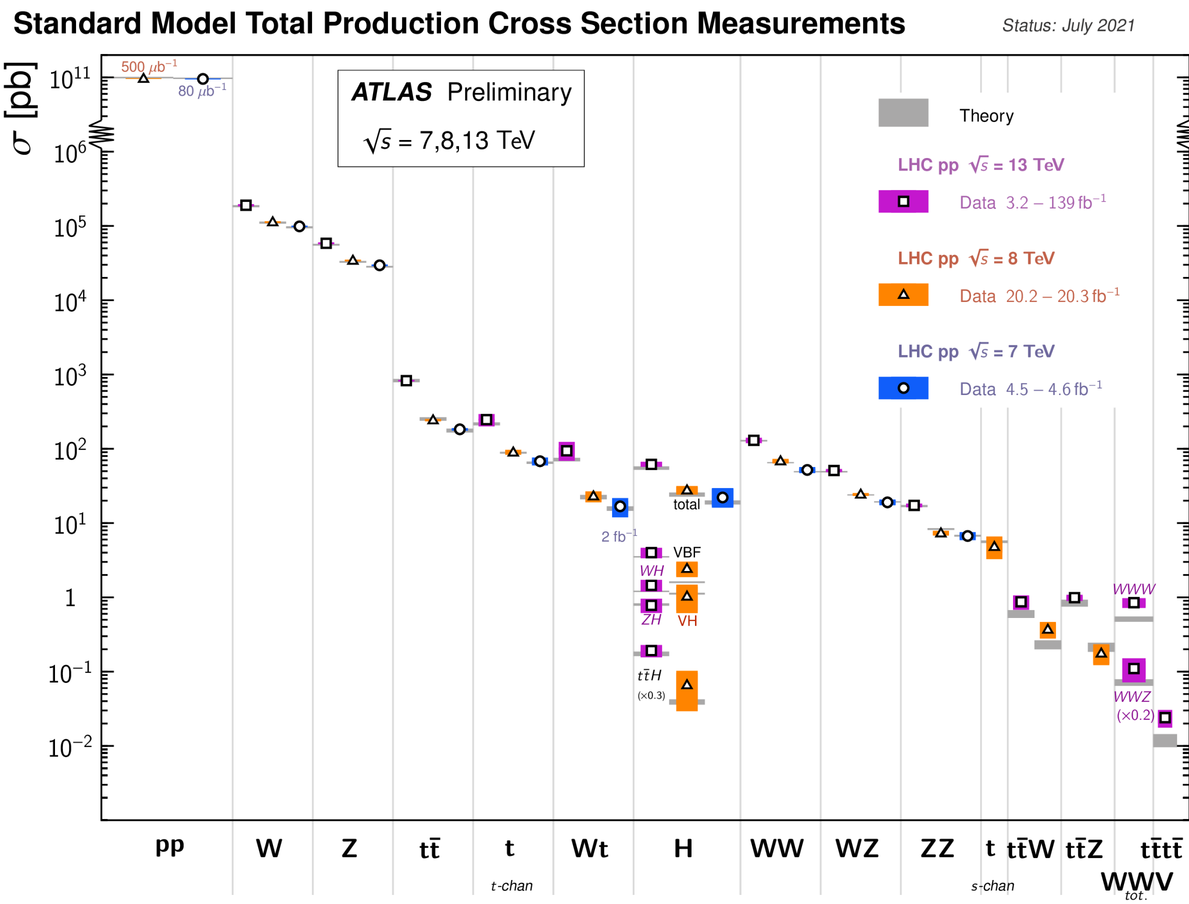

Figure 2.2: Production cross sections of different final states measured by the ATLAS experiment at the LHC. Comparison with the SM theory predictions is also shown [34].

Chapter 3

The LHC and the ATLAS experiment

The Large Hadron Collider (LHC) is the world's most energetic particle accelerator and the ATLAS experiment is used to record the results of particle collisions at the LHC. In this chapter, details about both that are necessary to understand the High-Luminosity LHC upgrade project and the ATLAS experiment NSW upgrade are presented.

3.1 The Large Hadron Collider

The LHC is an accelerator 27 km in circumference and located ∼100 m underground at the CERN laboratory near Geneva, Switzerland [1]. It has two beam pipes within which bunches of protons counter-circulate before being collided in the center of one of four major experiments, such as the ATLAS experiment (discussed in section 3.3). Protons are guided on the circular trajectory using 1232 superconducting dipole magnets capable of a maximum field of 8.33 T. Radio-frequency accelerating cavities are used to accelerate protons to a the maximum design energy of 7 TeV [35]. During LHC Run-1 (2011-2012), protons were collided at a collision center-of-mass energy of 7 TeV and 8 TeV [36]. During LHC Run-2 (2015-2018), the center-of-mass energy of proton collisions was increased to 13 TeV [37], close to the maximum design value of 14 TeV [35]. It is not actually the protons that interact, but the constituent quarks and gluons that each carry some fraction of the energy and momentum of the collisions.

Luminosity

The number of proton-proton interactions generated by the LHC directly affects the statistics available to make measurements of interaction cross sections. Predicting the number of proton-proton interactions requires defining a metric called luminosity [11]. The luminosity of a particle collider is the number of particles an accelerator can send through a given area per unit time. It is calculated from the measurable quantities in Equation 3.1:

$$\mathcal{L} = \frac{f N_1 N_2}{4\pi\sigma_x\sigma_y} \, , \tag{3.1}$$

where f is the frequency of the bunch crossings (25 ns), N_1 and N_2 are the number of protons in each bunch ($\sim 10^{11}$ protons / bunch), and σ_x and σ_y are the RMS of the spatial distributions of the bunch. Therefore, luminosity is a property of accelerator beams, which are set by the capabilities of the accelerator. The design luminosity of the LHC was 10^{34} $\mathrm{cm}^{-2}\mathrm{s}^{-1}$. The units of luminosity are an inverse area; multiplying the luminosity by the cross section of a given process gives the expected rate for that process.

Integrating the *instantaneous* luminosity (equation 3.1) over a period of data collection time gives the integrated luminosity,

$$L = \int \mathcal{L}\,(t)\ dt \tag{3.2}$$

which is related to the total number of interactions. In this way, the luminosity is the link between the accelerator and the statistical power of measurements to be made with the data collected. So far, the LHC provided an integrated luminosity of 28.26 fb^{-1} in Run-1 [36] and 156 fb^{-1} in Run-2 [37].

3.2 The High-luminosity LHC

At the end of the LHC program in 2025, the statistical gain on measurements in running the LHC further will become marginal. The High-Luminosity LHC (HL-LHC) [2] project consists of the upgrade of the LHC infrastructure to achieve a nearly ten fold increase in instantaneous luminosity, thereby improving measurement statistics as well. Also, some systems will need repair and replacement to operate past ∼2020. The LHC will continue to be the most energetic accelerator in the world for years to come and is the only accelerator capable of directly producing the Higgs boson and top quarks. Therefore, the European Strategy for Particle Physics made it a priority "to fully exploit the physics potential of the LHC" with "a major luminosity upgrade" [38]. The goal is for the HL-LHC to provide an integrated luminosity of 3000 fb^{-1} in the 12 years following the upgrade. The luminosity

Figure 3.1: The LHC/HL-LHC timeline [39]. The integrated luminosities collected and projected for each run of the LHC are shown in blue boxes below the timeline and the center of mass energy of the collisions is shown in red above the timeline. The top blue arrow labels the run number. The acronym "LS" stands for "long shutdown" and indicates periods where the accelerator is not operating. During the shutdowns, upgrades to the LHC and the experiments are taking place. This timeline was last updated in January, 2021, and reflects changes in the schedule due to the ongoing pandemic.

actually achieved will depend on a combination of technological advances and upgrades in progress that affect the factors contributing to luminosity defined in equation 3.1 [2]. Figure 3.1 shows the projected schedule of the HL-LHC upgrades and operation [39].

One of the most anticipated measurements at the HL-LHC is the value of the triple-Higgs coupling. Measuring the coupling will allow the determination of the shape of the Higgs potential responsible for electroweak symmetry breaking. Any discrepancy with respect to the SM prediction will show that there must be other sources of electroweak symmetry breaking, and hence physics phenomena beyond the SM. The LHC is the only accelerator where the Higgs can be produced directly. The HL-LHC upgrade is required to produce a significant sample of Higgs produced in pairs to make a statistically meaningful measurement [3, 40]. Accordingly, detector sensitivity to various Higgs decays will be important at the HL-LHC.

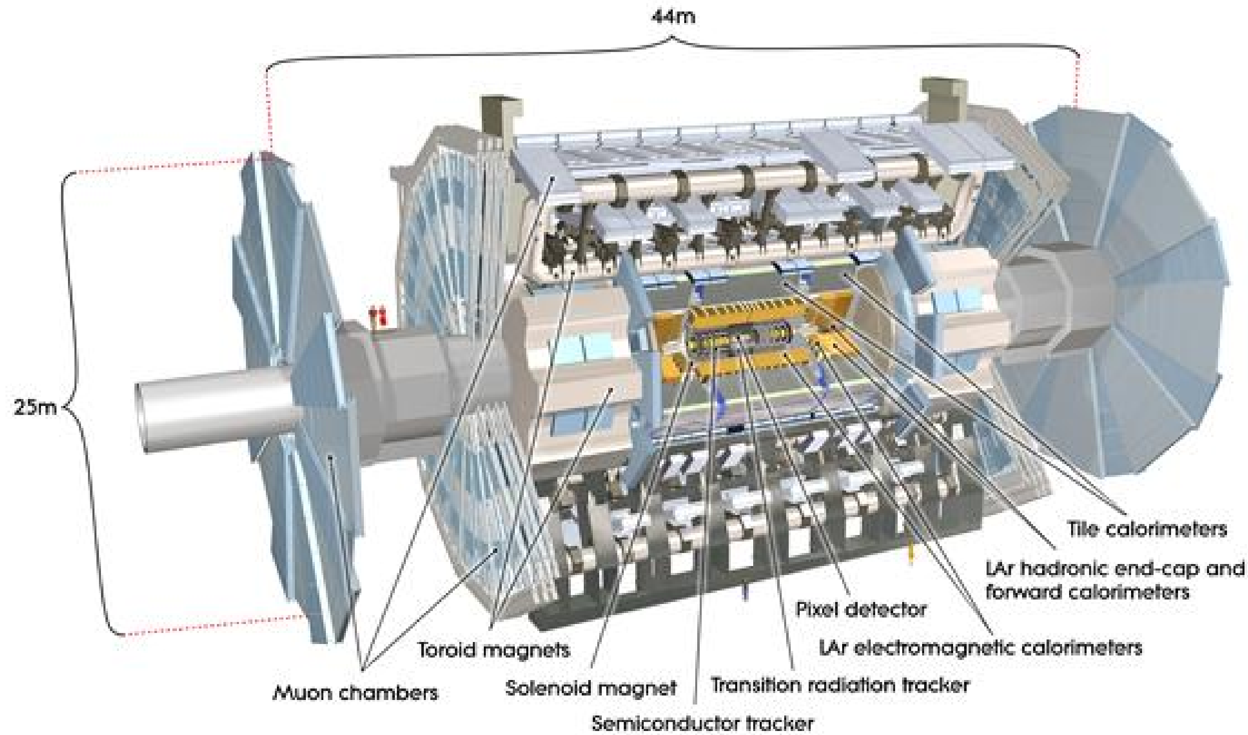

Figure 3.2: Diagram of the ATLAS experiment, with the various detector subsystems labelled [4].

3.3 The ATLAS experiment

The ATLAS experiment [4] was designed to support all the physics goals of the LHC. It is 44 m long and 25 m in diameter, and weighs 7000 tonnes. The ATLAS experiment is centered around one of the LHC's interaction points (a place where the beams collide). As shown schematically in figure 3.2, ATLAS consists of an array of particle detector subsystems arranged concentrically around the beam pipe. The ATLAS experiment is cylindrical because it aims to provide 4π coverage around the interaction point. In reference to the cylindrical geometry of the experiment, it is helpful to separate the subsystems of ATLAS into the so-called "barrel" and "endcap"/"forward" regions.

For analysis purposes, a spherical coordinate system is defined. The azimuthal angle ϕ is measured around the beampipe and the polar angle θ is measured from the beam pipe. The polar angle is more often expressed in terms of pseudo-rapidity, defined as $\eta = -\ln\tan(\theta/2)$.

Pseudo-rapidity values vary from 0 (perpendicular to the beam) to $\pm\infty$ (parallel to the beam, defined as the z-direction). Pseudo-rapidity is an approximation to the rapidity of a particle when its momentum is much greater than its mass. It is useful to describe the direction of outgoing particles in proton-proton collisions because differences in rapidity are invariant to a Lorentz boost along the beam direction.

The ATLAS experiment provides identification and kinematic measurements for each particle created after the initial collision by assembling offline the information recorded by each subsystem of ATLAS. With this information, signatures of processes of interest can be identified and studied. An overview of the main ATLAS subsystems is given below.

The inner detector

The inner detector [41, 42] (figure 3.3) is for precise measurements of charged particle trajectories, measurement of primary and secondary interaction vertices and to assist in the identification of electrons. A 2 T solenoid with field parallel to the beam bends the trajectory of outgoing charged particles. A measurement of the bending radius of each charged particle provides information about its momentum. The innermost part of the inner tracker is made of high-resolution semiconductor pixel and strip detectors while the outermost part is made of straw-tubes. The straw tubes are used in the trajectory measurements but they are also interspersed with material designed to enhance the creation of transition radiation. Transition radiation occurs when a highly relativistic charged particle traverses a material boundary [43]. The amount of transition radiation emitted by a charged particle is detected by the straw-tubes and is used to identify electrons.

that generate and detect transition radiation

Calorimetry system

Electromagnetic and hadronic sampling calorimeter units are used to record the energy of electrons, photons and jets[1]. A combination of liquid-argon (LAr) electromagnetic and hadronic calorimeters [44] and tile-scintillator hadronic calorimeters [45] cover the rapidity range $|\eta| < 4.9$, as shown in figure 3.4.

Sampling calorimeters have alternating layers of dense material and material that can measure the amount of ionization by charged particles. The dense material causes incoming charged particles to shower into lower energy particles and deposit their energy in the sensitive volume. Only muons and neutrinos are known to pass the calorimeters to the muon spectrometer without being absorbed.

[1] When quarks or gluons are expelled in a high energy collsion, they create collimated groups of hadrons because of the nature of the strong force [43].

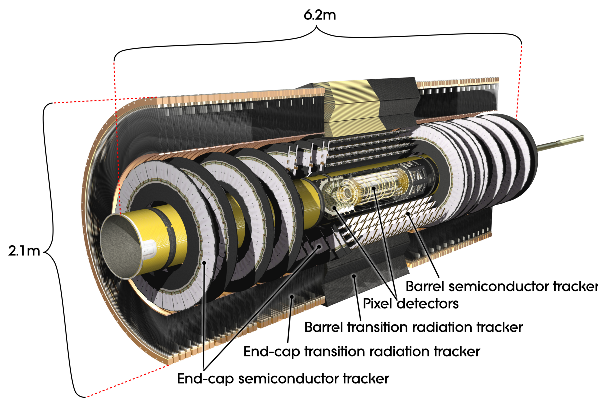

Figure 3.3: Schematic diagram of the ATLAS experiment's inner detector, with the different segments and the technology used labelled [4].

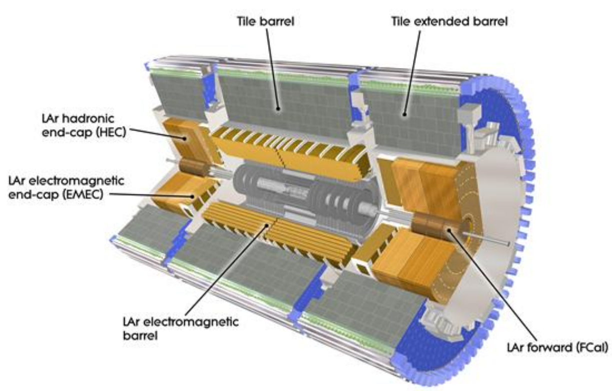

Figure 3.4: Schematic diagram of the ATLAS calorimeter system, with the different segments and the technology used labeled [4].

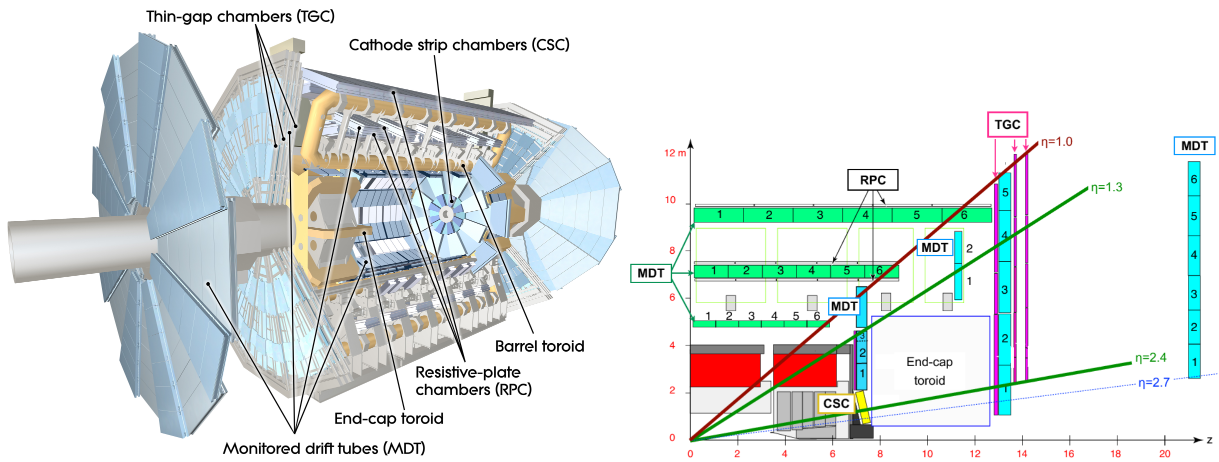

(a) (b)

Figure 3.5: Schematic diagram of the ATLAS muon spectrometer. Figure (a) shows a 3D projection of the system with the different types of chambers and different parts of the toroidal magnet system labeled [4]. Figure (b) shows a projection of one quarter of the muon spectrometer, with the interaction point in the bottom left corner. The small wheel is just left of the end cap toroid, the big wheel is to its right, and the outer wheel is the rightmost structure [48].

Muon spectrometer

The muon spectrometer [46] consists of multiple layers of tracking chambers embedded in a 2 T magnetic field generated by an air-core superconducting toroid magnet system. Figure 3.5a shows a schematic diagram of the layout of the different chambers and of the toroid magnets [4]. The trajectory of a muon is reconstructed from the information recorded by the different types and layers of tracking chambers. The amount of bending in the magnetic field provides a measure of the muon's momentum. In the barrel section of ATLAS, the toroidal magnetic field is created by eight coils bent into the shape of a "race-track" and symmetrically arranged around the beampipe. In the forward region, two end-cap toriods, each with eight smaller racetrack-shaped coils arranged symmetrically around the beam pipe are inserted in the ends of the barrel toroid [47].

The muon spectrometer is separated into detectors used for precision offline tracking and for triggering purposes. Three layers of monitored drift tubes (MDTs) or cathode strip chambers (CSCs) are used for tracking. The position of the muon track in each of the three layers allows reconstruction of the bent trajectory of a muon and hence its momentum. To satisfy the muon spectrometer target momentum resolution of $\Delta p_T/p_T < 1{\times}10^{-4}\ p$ / GeV for $p_T < 300$ GeV and a few percent for lower p_T muons, the MDTs and CSCs were designed to achieve a spatial resolution of 50 µm each. Accordingly, an optical alignment system was designed to monitor and correct for chamber positions [46, 49].

Resistive plate chambers (RPCs) are used for triggering in the barrel and thin-gap chambers (TGCs) are used for triggering in the endcaps. The positions of each type of chamber are sketched in figure 3.5b. The endcap section of the muon spectrometer consists of three sections, the small wheel, big wheel, and outer wheel – ordered by proximity to the interaction point. In Run-1, low (high) p_T muons were triggered on at L1 if two (three) of the RPCs or TGCs layers around the big wheel fired in coincidence, for the barrel and endcaps respectively [50]. After Run-1 it was discovered that up to 90% of the triggers in the endcap were fake, caused by background particles generated in the material between the small wheel and the big wheel [5]. To reduce the fake rate in Run-2, the TGCs on the inside of the small wheel also had to register a hit. The added condition reduced the trigger rate by 50% in the range $1.3 < |\eta| < 1.9$ [51]. The effectiveness of the solution was limited since the $|\eta|$-range of the small wheel TGCs was limited to $1.0 < |\eta| < 1.9$ and the position resolution of the small wheel TGCs is coarse [5].

Trigger system

It would be impossible to record all the data from bunch crossings every 25 ns, corresponding to a rate of ∼40 MHz. The ATLAS experiment has a multi-level trigger system to select events of interest for permanent storage. The Level-1 (L1) hardware trigger [50] uses partial-granularity information from the muon spectrometer and calorimeters to trigger on high p_T muons, electrons, jets, missing transverse energy, and τ decaying to hadrons. After Run-3 an upgrade of the trigger system will allow a maximum trigger rate of 1 MHz with a latency of 10 µs [52], but for now the working limits are a rate of 100 kHz [51] and 2.5 µs [50].

The L1 trigger is used to define regions of interest that are fed into the software high level trigger (HLT) [53], in which the full granularity of the muon spectrometer and calorimeter are used with information from the inner detector to reduce the trigger rate to 1 kHz. Events that satisfy at least one of the L1 and HLT trigger criteria are recorded to permanent storage for offline analysis.

With the foreseen increase in luminosity at HL-LHC, it is a priority to upgrade the ATLAS detector to further reduce the muon trigger fake rate in the forward region. The New Small Wheels being commissioned to replace the original ATLAS muon small wheels will address this challenge.

Chapter 4

The New Small Wheels

4.1 Motivation for the New Small Wheels (NSWs)

The hit rate of all detector systems will increase with the HL-LHC not only because of the increase in luminosity, but also because the background radiation rate increases proportionally with luminosity. The combined rate presents problems for both the tracking and triggering capabilities of the muon spectrometer [5].

In term of tracking, the efficiency of the MDTs decreases by 35% (mostly due to long dead-times) already when exposed to the maximum hit rate at the current luminosity, 300 kHz. At the threefold increase in luminosity predicted for Run-3, most of the small wheel will be subjected to a hit rate well above 300 kHz and it will begin missing hits. Losing hits in the small wheel will reduce the high p_T muon momentum resolution. The decrease in resolution will affect the ability to search for, for example, the decay of heavy bosons (W', Z') or a pseudo-scalar Higgs predicted by some SUSY models [3].

Already, the forward muon trigger system copes with a very high fake rate, even when including TGC data from the small wheel in the trigger as in Run-2. At the luminosity expected in Run-3, 60 kHz of the maximum 100 kHz of the L1 trigger would be taken by the endcap muon spectrometer. A possible solution would be to raise the minimum p_T threshold from 20 GeV to 40 GeV, but the ability to study several physics processes of interest depend on low p_T muons, particularly the Higgs decay to two muons, the Higgs decay to two tau's and SUSY particle decays to leptons [5].

The NSWs will solve both these problems. It will be covered with precision tracking chambers suitable for the expected hit rates and triggering chambers capable of 1 mrad angular

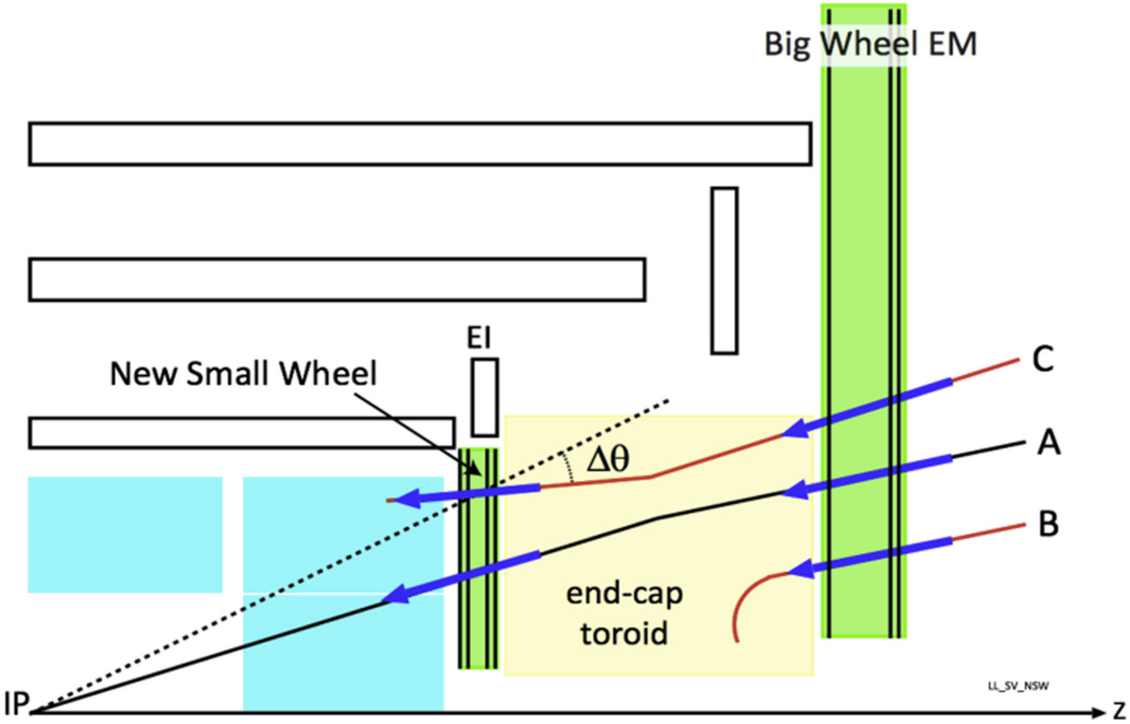

Figure 4.1: A schematic of a quarter cross section of the ATLAS detector, with the collision/interaction point (IP) in the bottom left corner. Three possible tracks are labelled. Ideally, track A would be triggered on while track B and C discarded. With the small wheel, all three tracks would be recorded. With the NSW, only track A would be recorded [5].

resolution. The idea behind the triggering chambers is to match the small wheel track segment with the track segment from the big wheel to discard tracks not originating from the interaction point. Figure 4.1 illustrates this point: the Run-1 trigger system would have triggered on all three tracks, while with the NSW the trigger system would only trigger on track A. Reducing the fake trigger rate means the NSWs will not miss as many muon hits and that the low p_T threshold will not have to be raised to cut particles not produced in the collision. The NSWs allow ATLAS to maintain the high p_T muon resolution and the low muon p_T threshold at the HL-LHC collision rate [5].

4.2 Design of the NSWs

The NSWs are covered with two detector technologies: micromegas and small-strip thin gap chambers. MMs are the primary tracking detectors and sTGCs are the primary triggering detectors, but for redundancy sake both are designed to do either. Both sets of detectors are to have position resolution better than ~100 µm per plane. Four chambers of each type are glued together to create quadruplet modules. Quadruplets of different sizes are assembled into wedges. Two sTGC wedges and two MM wedges are layered to create sectors (with the sTGC wedges on the outside) [5]. Different stages of the constrcution process are shown in figure 4.2. At the time of writing, both NSWs have been assembled. The first has been lowered into the ATLAS cavern and is being commissioned. The second will be lowered shortly.

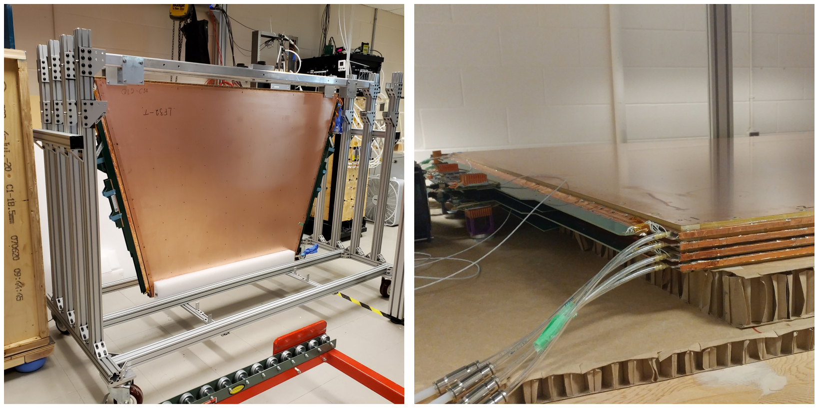

(a) An sTGC quadruplet module. The left image highlights the trapezoidal shape. The right image shows the short edge corner. The four sTGC layers and each layer's gas inlet are visible. The gas outlets and high voltage cables are at the long edge in the back of the photo. The green printed circuit board along the sides are the adaptor boards where the front end electronics are attached.

(b) Left: An sTGC wedge. The white frame outlines the individual quadruplet modules. Right: A completed sector, with two sTGC wedges on the outside and two MM wedges on the inside.

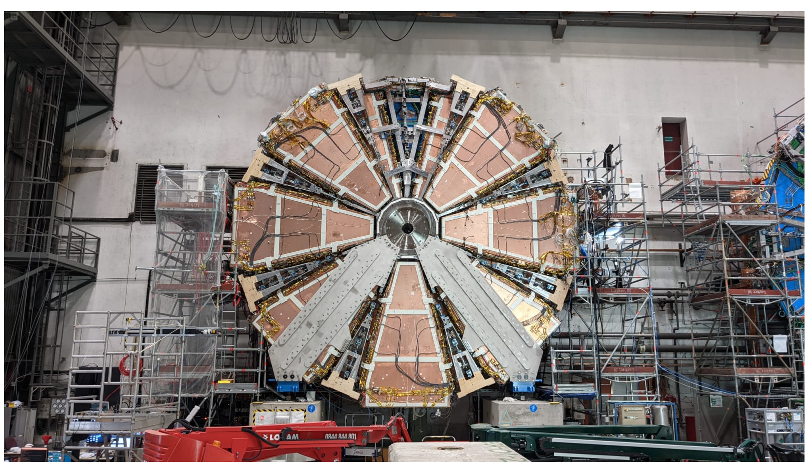

(c) The New Small Wheel. All sectors except one large sector at the top are installed, revealing two of the smaller sectors that are normally hidden under the large sectors and support bars. The NSWs are 10 m in diameter.

Figure 4.2: Images breaking down some of the construction units of the NSWs.

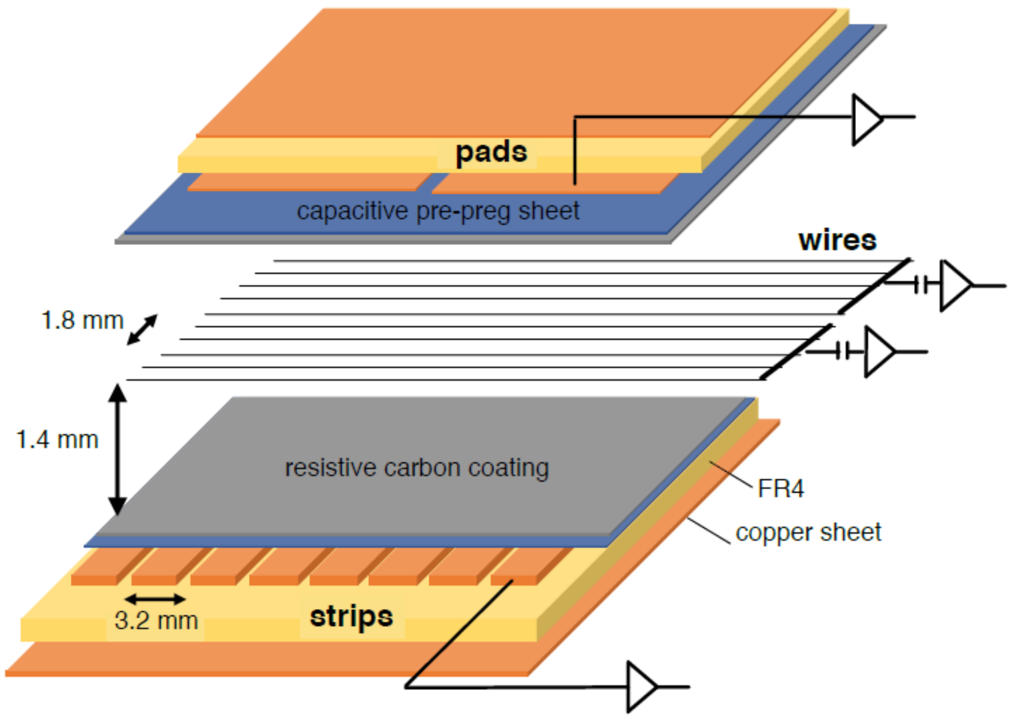

Figure 4.3: Interal structure of an sTGC, zoomed into the area under a pad. High voltage is applied to wires suspended in the gas volume to create an electric field. A passing muon causes an ionization avalache that is picked up by the wire, strip and pad electrodes [8].

4.3 Small-strip thin gap chambers

sTGCs are gas ionization chambers operated with a CO_2:n-pentane ratio of 55:45. Gold-plated tungsten wires, 50 µm in diameter and with 1.8 mm pitch, are suspended between two cathode planes made of FR-4, each 1.4 mm away (see figure 4.3). One cathode board is segmented into pads of varying area (around 300 cm^2 each), and the other segmented into strips of 3.2 mm pitch, perpendicular to the wires. High voltage is applied to the wires and the cathode planes are grounded [5, 54]. When a muon passes through, the gas is ionized and the electric field in the gas gap causes an ionization avalanche [55]. The motion of the ions and electrons are picked up on the nearby wire, strip and pad electrodes [5]. The gas mixture was chosen to absorb excess photons produced in the avalanche that delocalize the avalanche signal [56]. The resitivity of the carbon coating and capacitance of the pre-preg sheet tune the spread of the charge distribution [57] and the speed of the response [58] to optimize the rate capability. The hatching of the strips and wires establishes a coordinate system from which to extract the coordinate of the muon as it passes through the chamber. The small pitch of the strips is what allows the quadruplets to deliver good angular resolution to improve the fake trigger rate and meet the precision tracking requirements [5].

A 3-out-of-4 coincidence in pad electrodes from each layer of a quadruplet define a region of interest where the strip and wire electrodes should be readout. The pad triggering scheme greatly reduces the number of electrodes that require read-out so that a track segment of the required angular resolution can be provided quickly enough to the hardware trigger [5].

Signal is readout from groups of successive wires, so the position resolution in the direction perpendicular to the wires is 10 mm. The wires give the symmetric azimuthal coordinate in ATLAS so the position resolution in this direction is sufficient. Good resolution on the η coordinate, perpendicular to the strips, is important [5]. The average single chamber position resolution in the strip coordinate was 45 µm for perpendicular muon tracks as measured in a test beam [6] – well within design specifications. When four sTGCs are glued together into a quadruplet the design angular resolution of 1 mrad in the strip coordinate is achievable [5, 54].

Therefore, sTGCs are able to meet the triggering and precision tracking goals they were designed for. To ensure they can deliver once installed in ATLAS, knowing the position of the strips to within their position resolution in the ATLAS coordinate system is necessary. The NSW alignment system, detailed in section 4.5, monitors the position of alignment platforms installed on the surface of the wedges. The alignment platforms are installed with respect to an external reference on the sTGCs: two brass inserts on each strip layer on one of the angled sides of each quadruplet (shown in figure 4.4). So the challenge of positioning the strips in ATLAS was separated into two steps: first, position the strips with respect to the brass inserts; second use the alignment system to position the alignment platforms. The next section provides some pertinent details on the sTGC construction process, with steps that affect the position of the strips with respect to the brass inserts highlighted.

4.4 sTGC Quadruplet Construction

Five countries were responsible for producing the sTGC modules of varying geometries for the NSW: Canada, Chile, China, Israel and Russia. Canada was responsible for 1/4 of the required sTGCs, of three different quadruplet geometries. The steps of the construction process in each country were similar [5]. The process followed in Canada is detailed.

TRIUMF in Vancouver, British Columbia was responsible for preparing the cathode boards. The boards were made and the electrodes etched on at a commercial laboratory, Triangle

(a) Brass insert near long edge. (b) Brass insert near short edge.

Figure 4.4: The brass inserts sticking out from the gas volumes of an sTGC quadruplet. These inserts were pressed against alignment pins when the individual sTGCs were being glued together.

Labs, in Carson City, Nevada. Once completed they were sent to TRIUMF to be sprayed with graphite and otherwise prepared [7]. The boards are commercial multilayer printed circuit boards, but the strip boards required precision machining to etch the strip pattern [5]. Triangle Labs also machined the two brass inserts into each strip board. A coordinate measuring machine (CMM) was used to digitize a set of reference strips. Four quality parameters describing non-conformities in the strip pattern of each board with respect to the brass inserts were derived from the data and the results are available on a QA/QC database. The parameters and the CMM data collection is described in full in [7]. Due to time constraints, tolerances on the non-conformities in the etched strip pattern with respect to the brass inserts were loosened, with the condition that the strip positions in ATLAS would have to be corrected for [7].

The prepared boards were sent to Carleton University in Ottawa, Ontario for construction into sTGCs and quadruplets. First, the wires were wound around the pad cathode boards using a rotating table and the wires were soldered into place. A wound pad cathode board was held by vacuum on a granite table, flat to within 20 µm, and a strip cathode board glued on top to create an sTGC. Holding one sTGC flat with the vacuum, another was glued on top to create a doublet, then two doublets were glued together to create a quadruplet. When gluing sTGCs together, the brass inserts were pushed against alignment pins with the goal of keeping the strip layers aligned within tolerance. However, non-conformities in the shape of the brass inserts, non-conformities in the position of the alignment pins and shifts between sTGCs while the glue cured resulted in misalignments between the brass inserts and strip layers. Precise alignment of the pad boards or wires with respect to the strip boards did not have to be so tightly controlled because pads do not measure the precision coordinate.

The Carleton team finished the quadruplets by installing adaptor boards on the angled sides of each layer that allow front end electronics to be attached. Completed quadruplets were sent to McGill University where they were characterized with cosmic rays. The details of cosmic ray testing are described in chapter 5. Tested quadruplets were sent to CERN where they were assembled into wedges and alignment platforms installed. The alignment platforms were installed using a jig positioned with respect to the brass inserts. Completed wedges were assembled into sectors then installed on the NSWs.

The quadruplet construction process had two steps where strip positions could be shifted off of nominal. At board-level, there could be non-conformities in the etched strip pattern with respect to the brass inserts, described by the four quality parameters [7]. At the quadruplet level, misalignments between the brass inserts and strips on different layers were introduced during the gluing. The result was that the brass inserts were not a reliable reference point and that the strips can be offset from their design position by up to hundreds of micrometers. Offsets in strip positions from nominal in Canadian quadruplets were shown to be random [7], so no one correction would suffice. The offsets must be measured and corrected for in the ATLAS offline software that does the precision tracking. Understanding the work ongoing to make measurements of offsets and correct for them requires understanding the strategy of the NSW alignment system.

4.5 NSW alignment

The idea of the NSW alignment system is presented in [5], but the details have only been presented internally so far. After the wedges are constructed, alignment platforms are installed on every sTGC quadruplet and optical fibres routed to them, as shown in figure 4.5. Light from the optical fibres will be monitored in real time by cameras (BCAMs) mounted on the alignment bars of the NSWs. The system will thus record the positions of the alignment platforms in the ATLAS coordinate system, accessible at any point during operation.

The original alignment scheme was to use the brass inserts as a reference between the alignment platforms and the individual strips, as shown in the solid arrows in figure 4.6 – this will no longer work. The position of the alignment platforms will be known thanks to the alignment system, so a different method to get the position of the strips with respect to the alignment platforms is currently in its final stages. It uses the yet-unmentioned x-ray dataset to calculate offsets of the strip pattern of an sTGC layer in a local area (local offset) with respect to the nominal geometry by analyzing the beam profile left by an x-ray gun attached to different positions on the alignment platforms. Effectively, the reference to the brass inserts is skipped, represented as the dashed line in figure 4.6. The alignment platforms provide the link to the nominal geometry because their position with respect to the strips can be calculated from the nominal geometric parameters assuming that the strips are perfectly etched and aligned. Cosmic muon track positions cannot be compared to the nominal geometry because the alignment platforms are not installed when cosmics data is collected, so there is no external reference to provide a link to the nominal geometry.

The x-ray method does not have the sensitivity to measure the offset of each strip from nominal, but instead the offset of the strip pattern in a local area around the position of the gun can be measured. *Local offsets* are used to build an alignment model for each strip layer. Formally defined, an alignment model is a set of parameters used to estimate the true position of a strip given its nominal position. The alignment model currently being worked on takes x-ray and CMM data as input to calculate an offset and rotation of each strip layer with respect to nominal [8]. The alignment parameters could be described as “global”, meaning over the whole layer instead of local. Without the x-ray dataset, there would be no input to the alignment model that takes into account inter-layer misalignments introduced

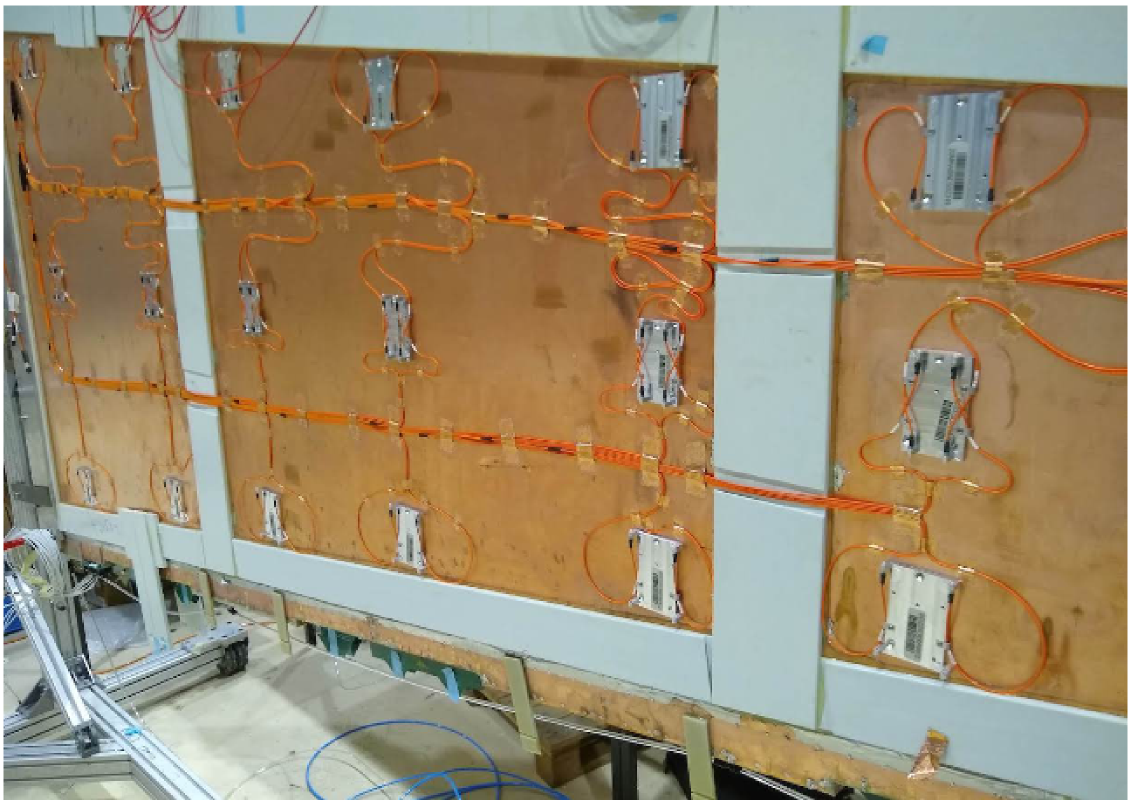

Figure 4.5: An sTGC wedge with alignment platforms (silver) installed on the quadruplet. Optical fibres (orange) are routed to the alignment platforms. Cameras on the frames of the NSWs will record light from the optical fibres to position the alignment platforms in the ATLAS coordinate system.

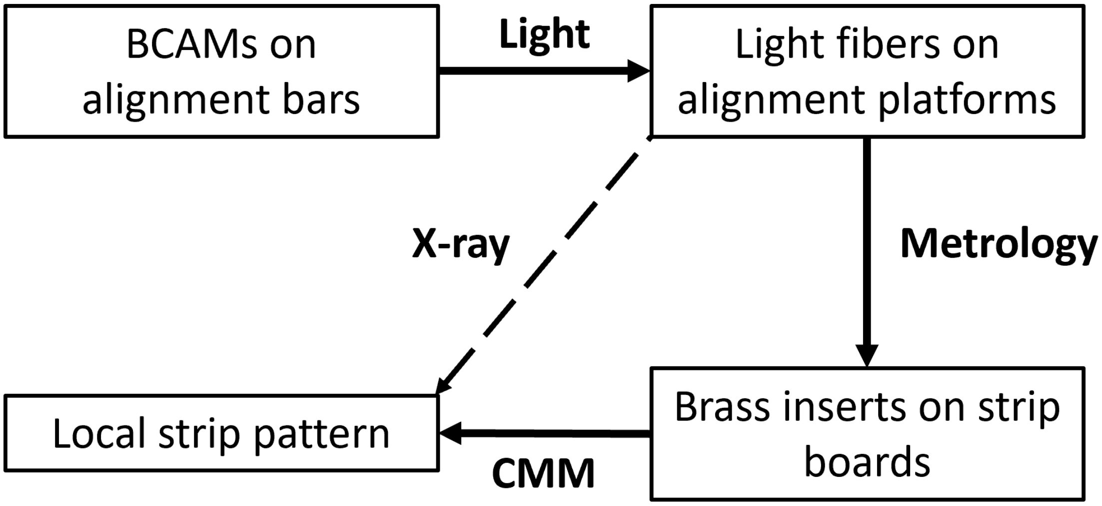

Figure 4.6: How the different elements of the sTGC alignment system relate to one another. The solid arrows denote the planned alignment scheme. The dashed arrow shows the modification being finalized now. This figure was originally designed by Dr. Benoit Lefebvre.

in construction.

Given that the x-ray local offsets can only be measured at positions where the gun can be attached and that they are an important part of the alignment scheme, the x-ray method needs to be validated. The goal of this thesis is to validate the x-ray local offsets while exploring how cosmics data complements and adds to the understanding of strip positions and overall alignment.

Chapter 5

Using cosmic muons to measure relative strip position offsets

At McGill, among other quality and functionality tests, each Canadian-made quadruplet was characterized with cosmic muons. In this chapter, the experimental setup and how the data was analyzed to provide relative strip position offsets is presented. The analysis method was motivated by the how it could be compared to data collected with the x-ray method (chapter 6) but also stands alone as a characterization of the alignment between strips of different layers. First, a brief introduction to cosmic rays.

5.1 Cosmic rays

The Earth is being bombarded by particles from the sun, galactic sources and extra galactic sources – collectively called cosmic rays [19, 11]. Cosmic rays are mostly protons, but also heavier ions, gamma rays and the term sometimes includes neutrinos. The primary (initial) cosmic ray interacts with the atmosphere causes electromagnetic and hadronic showers of particles. Hadronic showers result from the primary cosmic ray interacting strongly with the target of the atmosphere and the most abundant products are pions. Charge pions mostly decay to muons (there is a lesser contribution to the muon flux from kaons as well) [59]. Thanks to time dilation extending the muon's lifetime as measured on Earth, a flux of approximately 1 muon/cm^2/ min reaches the ground [11]. Measuring the muon flux and energy spectrum reveals information about primary cosmic rays [59] which is interesting to high energy physicists and astrophysicists. The muon flux is also terribly convenient for testing muon detectors.

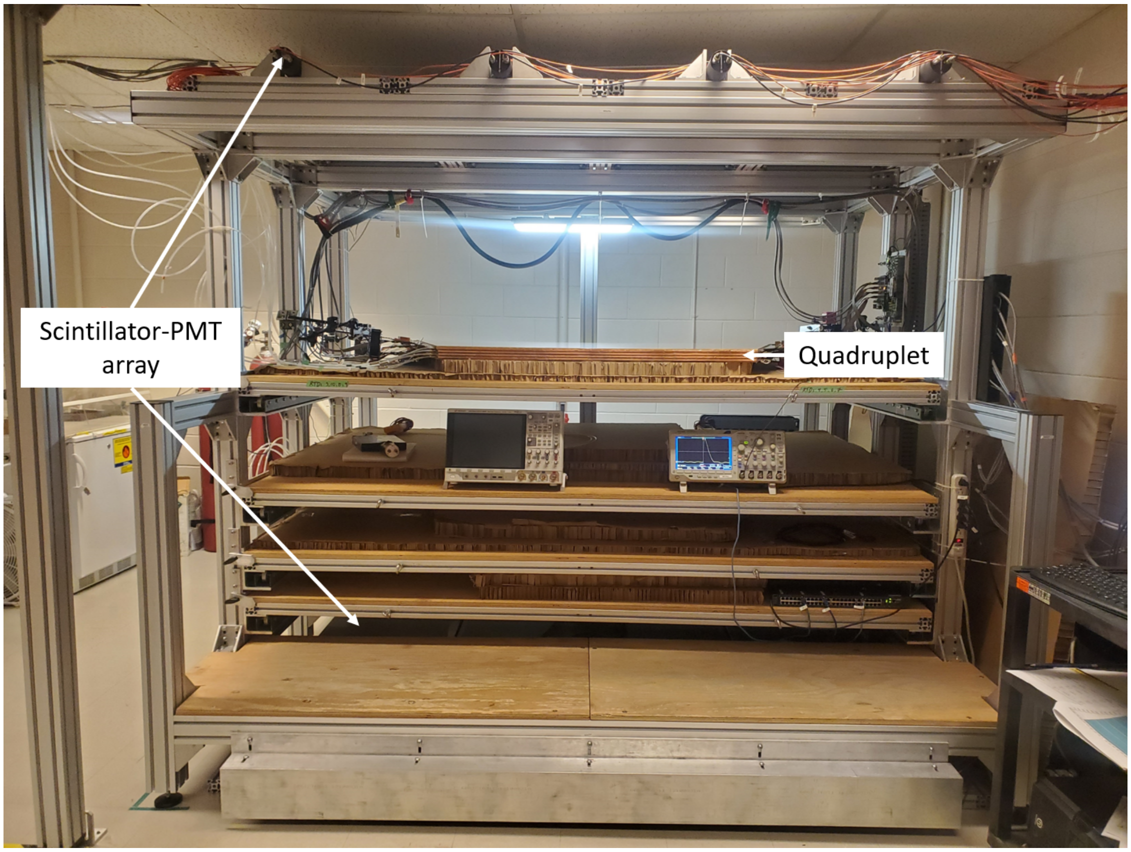

Figure 5.1: Cosmic muon hodoscope at McGill University with sTGC quadruplet in the test bench.

5.2 Experimental setup

Cosmic muon characterization was done with a hodoscope, a complete description of which can be found in [60]. The quadruplet was placed in the center of the test bench. Above and below it was a layer of scintillator-PMT arrays, labeled in figure 5.1. When a cosmic muon passed within the acceptance of the hodoscope, at least one scintillator from the top array and at least one from the bottom array fired in coincidence. The coincident signal was used to trigger the readout of the quadruplet's electrodes using NIM modules. The trigger was passed to the front-end electronics attached to the adaptor boards of each layer of the quadruplet.

Operating the chambers also required gas and high voltage. A pentane-CO_2 mixture was mixed and delivered to each sTGC with a gas system designed and made at McGill University.

The gas system was controlled by a slow control program, also made in-laboratory [61]. Although gas mixture is flammable, it allows the chambers to operate in high amplification mode without prodution of excess photons saturating the signal across many strips because pentane absorbs a wide energy of photons [56]. To prepare the quadruplets for operation, CO_2 was flushed through them overnight to remove impurities. Then, five gas volumes of the pentane-CO_2 mixture was flushed through (approximately 3 hours). High voltage was provided by CAEN boards.

5.3 Data acquisition

Each sTGC electrode was connected to a channel on a prototype ASIC[1] on the front-end electronics, attached to the adaptor boards on each layer of a quadruplet. The ASIC amplified the signal and was set to measure and record the signal peak amplitude from electrodes. For each trigger, the signal peak amplitude of all channels above threshold was recorded as an event and stored in a binary file. Channel thresholds were estimated [63] and adjusted manually in the configuration/readout software before the start of data acquisition. There was an exception to the threshold rule: the signals on strips adjacent to a strip above threshold were also readout using the so-called“neighbour triggering” function of the ASIC.

The quadruplets were held at 3.1 kV for approximately two hours to collect data from 1 million muon triggers.

5.4 Data preparation

5.4.1 Cuts on electrode hits

Corrupted data is removed while the raw data is being recorded in a binary file. The binary file is decoded into a usable `ROOT` [64] tree offline.

A hit is defined as a signal recorded from a channel that was above threshold or (in the case of strips) neighbour triggered. In addition to hits from muons, the quadruplets record noise from the electronics and δ-rays (electrons liberated with sufficient energy to cause more ionization before acceleration). Therefore, cuts are applied to reduce the number of noise hits. The edge strips are very noisy, so all strip hits on layers with strip hits on either edge channel are cut. A default pedestal value is subtracted from the recorded signal peak

[1] the VMM3 [62], designed for the MMs and sTGCs of the NSW

amplitude of each electrode for a more realistic estimate of the signal amplitude. Also, events that only have hits on pad electrodes (no strips or wires) were cut because the large area of the pads made them susceptible to noise.

5.4.2 Clustering and tracking

Many of the high-level characterization metrics require rebuilding muon tracks. For events passing quality cuts, the x- and y-coordinates of the ionization avalanche on each layer are extracted from the signal on the wires and strips respectively for each event, as is sketched in figure 5.2. In this work, x is the coordinate perpendicular to the wires and y is the coordinate perpendicular to the strips.

The x-coordinate is taken as the center of the wire group with the maximum peak signal amplitude, since the wire groups' pitch (36 mm) is larger than the typical charge spreading. Assuming that the true x-position of the hit is sampled from a uniform distribution over the width of the wire group, the uncertainty in the x-position was given by $\frac{36}{\sqrt{12}}\,\text{mm} = 10\,\text{mm}$ [65].

The y-coordinate is taken as the Gaussian mean of the peak signal amplitude distribution across groups of contiguous strips. The process of grouping contiguous strip hits on a layer is called clustering, and the resulting group is called a cluster. Figure 5.2 sketches the clustering process and a sample cluster is shown in figure 5.3. The data acquisition system recorded the electrode ID of the strip hit and in the clustering process the position of the center of the strip electrode is calculated based on the nominal quadruplet geometry. Typically, clusters are built of 3-5 strips. The thickness of the graphite coating over the cathode boards determined how many strips picked up the ionization image charge. Larger clusters were more likely caused by δ-rays since they spread the cloud of ionization.

Events are cut from the analysis if there are two clusters on one layer's set of strips (indicative of noise). Clusters are cut if the cluster size is lesser than three (which should not happen for real events thanks to neighbour triggering), and if the cluster size is greater than 25. After all the cuts on hits and clusters, roughly half as many muon tracks as triggers collected remain.

The uncertainty in the y-coordinate could have been taken as the fitted cluster mean's statistical uncertainty; however, after comparing the difference in cluster means for different fitting algorithms in appendix A.2, 60 µm of uncertainty was assigned.

The coordinates of the avalanches' on all layers were used to reconstruct tracks in x and y respectively. The tracks were then used to calculate characterization metrics like electrode efficiency and spatial resolution, the details of which are discussed in [60].

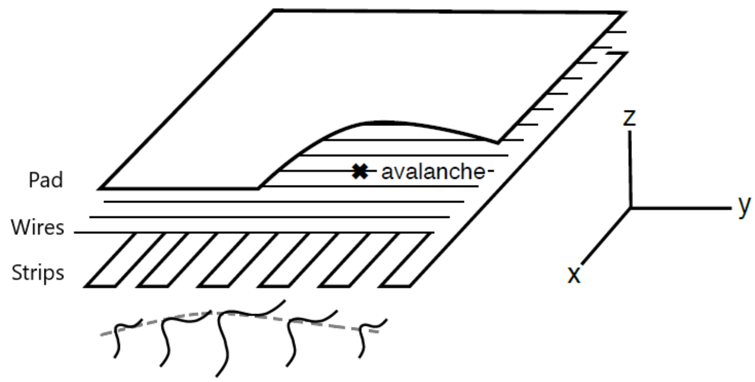

Figure 5.2: A sketch of an sTGC-like detector. The position of the avalanche is extracted from the wires and strips that picked up the avalanche signal. The signals on individual strips are sketched. Clustering was the processs of fitting a Gaussian to the peak value of the signals on individual contiguous strips, as is done in figure 5.3. In this work, the $x(y)$-coordinate will always refer to the coordinate perpendicular to the wires (strips) [60, 57].

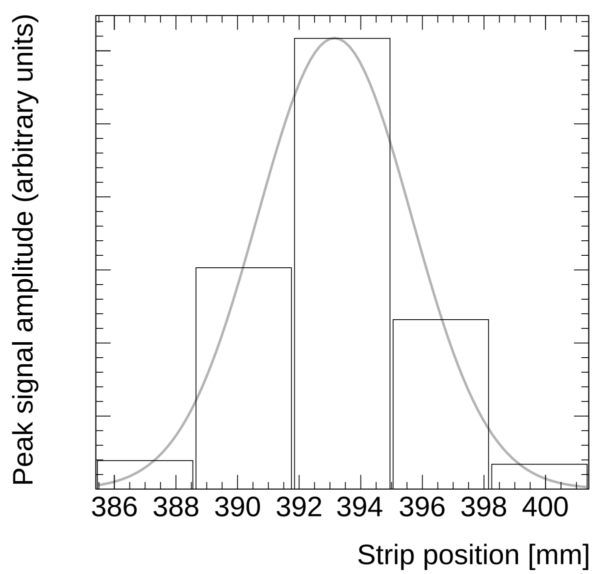

Figure 5.3: A sample cluster resulting from the current picked up on a group of strips after the passing of a muon (presumably). The grey curve is a Gaussian fit.

5.5 Measuring relative local offsets

The offset of a strip from its nominal position can be modeled as a passive transformation. For each area of a strip layer, the local offset is the shift of the strip pattern in that area with respect to the nominal geometry. Local offsets systematically change the set of strips nearest to muons passing through the area. The data preparation software assumes that strips are in their nominal positions, so the recorded muon y-position on layer i, y_i, is shifted opposite to the layer's local offset, $d_{local,i}$, by

$$y_i = y_{nom,i} - d_{local,i}, \tag{5.1}$$

where $y_{nom,i}$ is the position of the muon that would have been recorded on layer i if there was no local offset. Equation 5.1 ignores other factors that affect the cluster position, like position resolution. With cosmics data, the local offset is unknown and there was no external reference to measure $y_{nom,i}$. Therefore, only relative local offsets could be calculated.

The minimal relative coordinate system uses two reference or fixed layers [60]. The hits on the two fixed layers were used to create tracks that can be interpolated or extrapolated (polated) to the other two layers. The set of two fixed layers and the layer polated to are referred to as a tracking combination. The residual of track i, Δ_i is defined as,

$$\Delta_i = y_i - y_{track,i}, \tag{5.2}$$

where $y_{track,i}$ is the polated track position. Track residuals are affected by the relative local offset in the area of each layer's hit. As an example, in figure 5.4, the residual on layer 2 perhaps indicates that layer 2 is offset with respect to layers 1 and 4 in the area of the track. Of course, a single track residual says nothing of the real relative local offset because of the limited spatial resolution of the detectors and fake tracks caused by noise or delta rays. However, the mean of residuals for all tracks in a region will be shifted systematically by the local offsets between layers [60]. For a quadruplet with nominal geometry, the mean of residuals should be zero in all regions and for all reference frames, unlike the example regions in figure 5.5. The value of the mean of residuals is a measure of the relative local offset of the layer with respect to the two fixed layers.

To study the relative local offsets, residual distributions across each strip layer of a quadruplet for all tracking combinations were assembled and fitted. The residual distributions were wider for tracking combinations where the extrapolation lever arm was largest, as in the example distributions shown in figure 5.5. In general, residual means from distributions of residuals with geometrically less favourable tracking combinations have larger statistical and systematic uncertainties. The bin size of 200 µm for the distributions shown in figure 5.5 was

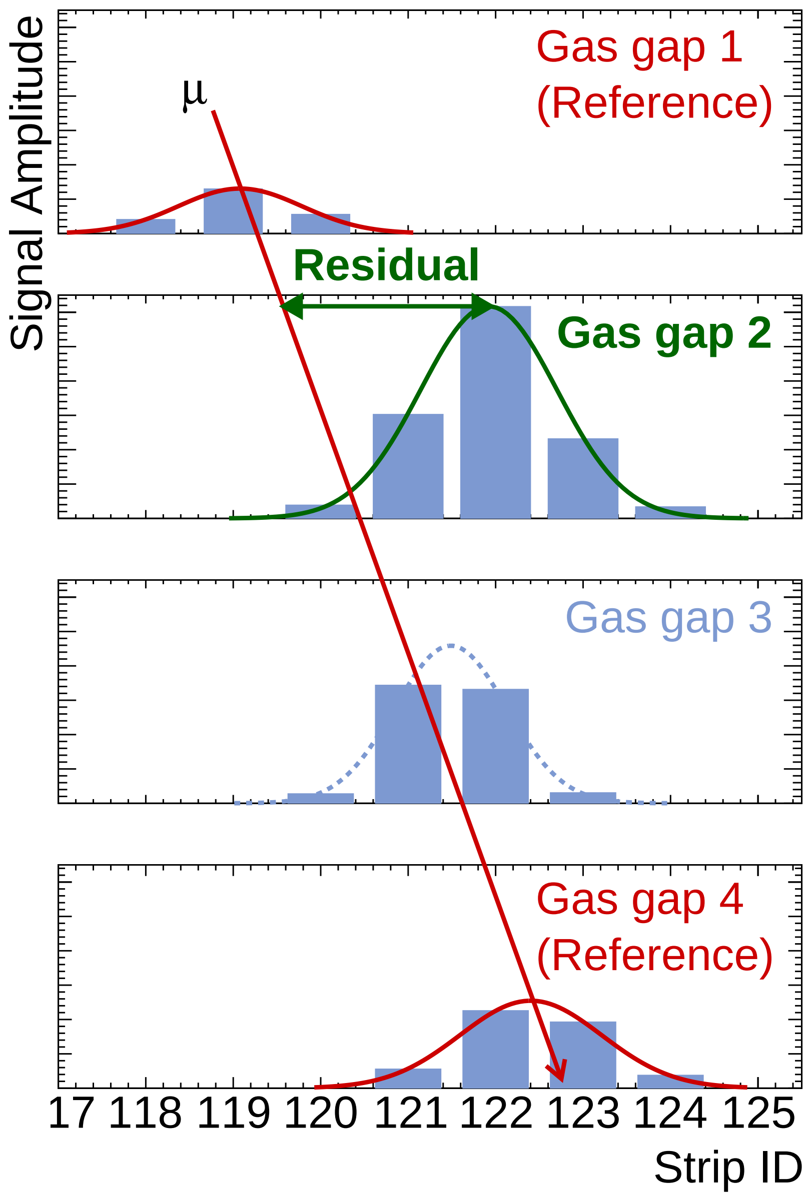

Figure 5.4: Representation of a muon event recorded by an sTGC. The clusters are fit with a Gaussian and the mean is taken as the hit position. A track is built from the chosen reference layers, 1 and 4, and the residual calculated on layer 2. The clusters come from a real muon, but their positions were modified to highlight the residual on layer 2.

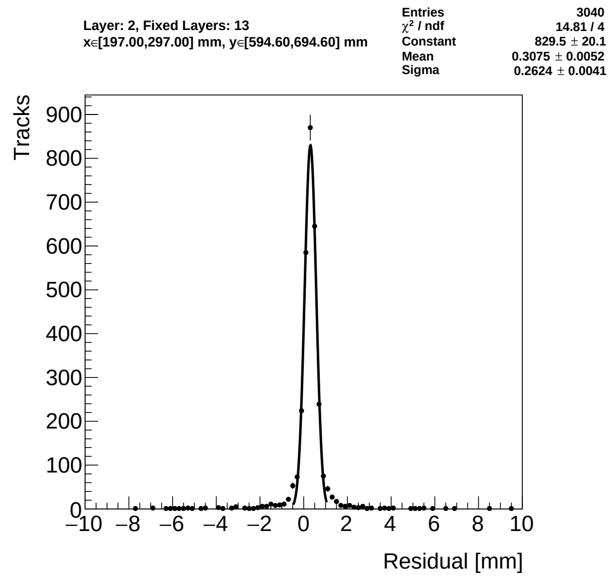

(a) Tracks on layer 2, reference layers 1 and 3.

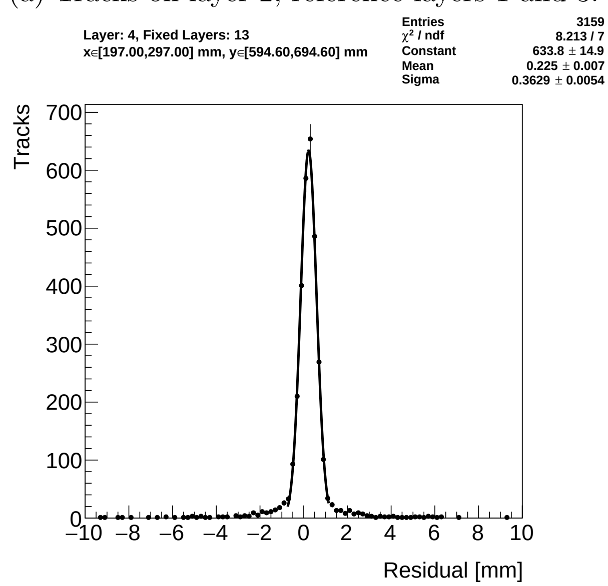

(b) Tracks on layer 4, reference layers 1 and 3.

Figure 5.5: Residual distribution in the region $x \in [197, 297]$, $y \in [594.6, 694.6]$ mm (100 mm by 100 mm area) for two different tracking combinations. Data from quadruplet QL2.P.11.

chosen based on the uncertainty on residuals calculated from tracks on layer 4 (1) built from hits on layers 1 and 2 (3 and 4) given a cluster y-position uncertainty of 60 µm (appendix A.3), since these tracks yield residuals with the largest uncertainties.

A gaussian fit was used to extract the mean of the residual distributions. Theoretically, a double gaussian distribution is more apt, but for this analysis the gaussian fit was sufficient, as discussed in appendix C.1.

The area of the region of interest was 100 mm by 100 mm. The size balanced the amount of tracks falling in the region of interest to give a small statistical uncertainty on the extracted mean while being smaller than the order on which local offsets were expected to change significantly. The change in local offsets over the surface of a layer can be modeled using global alignment parameters. Using a base alignment model with a global offset and rotation of each strip layer, "significantly" was defined by the distance in x that a large but possible rotation of 1000 µrad would change the local offset by more than 50 µm – half the required position resolution of the sTGCs [5].

5.6 Visualizing relative alignment between layers

The mean of residuals was plotted across entire strip layers for every tracking combination to get a picture of the how relative local offsets change over the layers' surface. Figure 5.6 shows the mean of residuals on layer 2 with reference layers 1 and 3 for two different quadruplets, referred to as QL2.P.11 and QL2.P.8, for 100 mm by 100 mm areas across the surface of layer 2. To understand these plots, realize that the Gaussian mean of the distribution in figure 5.5a is the entry in area bin $x \in [197, 297]\,, y \in [594.6, 694.6]$ mm in figure 5.6a.

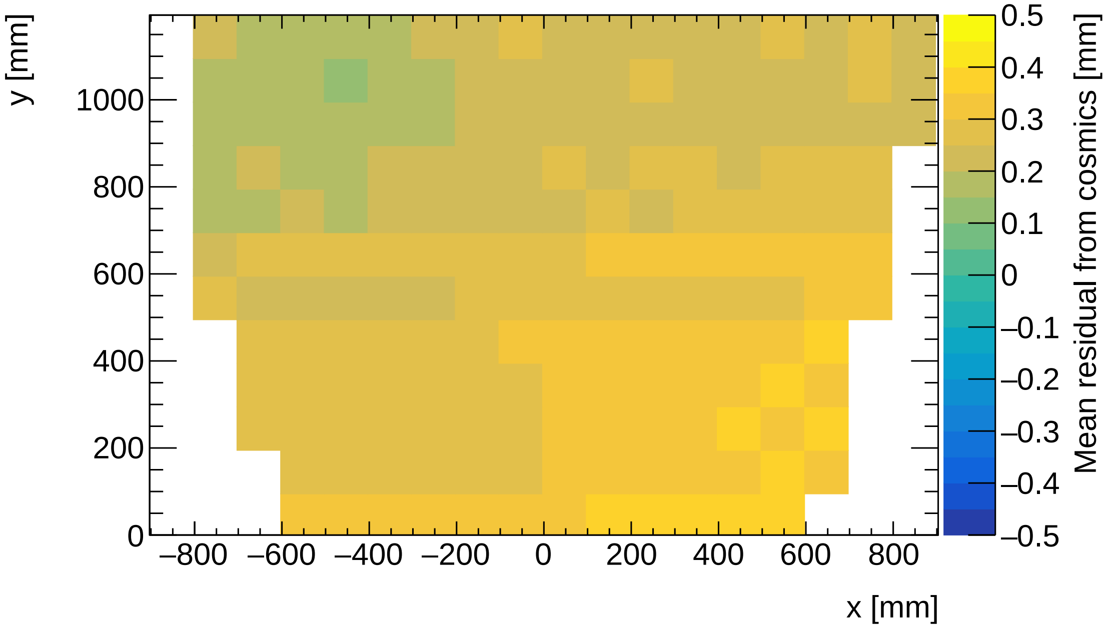

(a) Mean of residuals of tracks on layer 2, reference layers 1 and 3, for QL2.P.11.

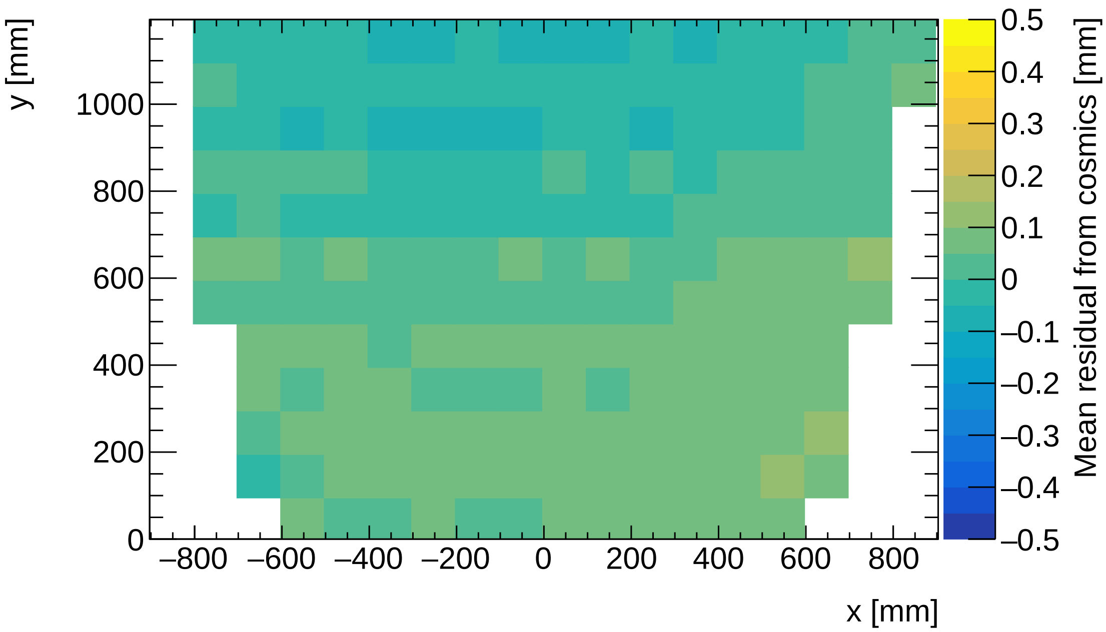

(b) Mean of residuals of tracks on layer 2, reference layers 1 and 3, for QL2.P.8.

Figure 5.6: Mean of residuals in each 100 mm by 100 mm bin over the area of the layer 2 cathode board. The entry in $x \in [197, 297]$, $y \in [594.6, 694.6]$ mm of figure 5.6a corresponds to the fitted Gaussian means in figures 5.5a. The mean of residuals is an estimate of the local offset of layer 2 with respect to layers 1 and 3.

Many of the residual means are non-zero and change smoothly over the layer, indicating that there are relative local offsets stemming from misalignments between entire strip layers. Given that the residual mean changes with x in figure 5.6a, there is likely a rotation of layer 2 with respect to layers 1 and 3 on QL2.P.11, combined with an offset of the entire layer. The residual means are smaller in figure 5.6b indicating that QL2.P.8 is less misaligned overall than QL2.P.11; however the relative local offsets range between $\pm 200\,\mu\text{m}$ so they are still significant considering the order on which the chambers must be sensitive to position, $\sim 100\,\mu\text{m}$.

5.7 Systematic uncertainty

The statistical uncertainty on the local residual means was typically around 10 - 20 µm, and appendix B shows that the analysis was not statistically limited by the number of triggers collected for each quadruplet. The systematic uncertainties were more significant.

Systematic uncertainties were assigned per tracking combination as the RMS of the distribution of the difference in local residual means each calculated in a different way. For example, the RMS associated with fitting the local residual distributions with a Gaussian or double Gaussian is 25 µm for the geometrically least favourable tracking combinations. The distribution is shown in appendix C.1. For geometrically similar tracking combinations (like: tracks on layer 1 built from hits on layers 3 and 4, and tracks on layer 4 built from hits on layers 1 and 2), the systematic uncertainty was assigned as the average RMS of both.

Other choices were: whether to use data collected at 2.9 kV or 3.1 kV (both are collected at McGill); what cluster fitting algorithm to use; and whether or not to apply a differential non-linearity (DNL) correction to the cluster y-positions. A systematic uncertainty was assigned using the method above to account for the effect of each choice and quantify the robustness of the mean of residuals. The reasons for each choice are listed below.

Data taken at 3.1 kV was used over 2.9 kV because the strip and wire tracking efficiency increases with higher voltage [60] (appendix C.2).

The `Minuit2` package [66] was used to fit clusters over Guo's method [67] because it provided automatic statistical uncertainty estimates and is the standard fit algorithm of `ROOT` [64] (appendix C.3).

The DNL correction was not applied because its effect on the residual means was negligible (appendix C.4).

A summary of the systematic uncertainties assigned for each tracking combination is given in table 5.1.

Tracking geometry	**Residual distribution fit function (C.1)**	**Cosmics data collection voltage (C.2)**	**Cluster fit algorithm (C.3)**	**Apply DNL correction or not (C.4)**	**Total**
Similar to layer 3, fixed layers 1, 2	0.01	0.04	0.02	0.01	**0.05**
Similar to layer 4, fixed layers 1, 2	0.03	0.01	0.03	0.01	**0.10**
Similar to layer 2, fixed layers 1, 3	0.01	0.02	0.01	0.000	**0.03**
Similar to layer 4, fixed layers 1, 3	0.01	0.04	0.01	0.01	**0.04**
Similar to layer 2, fixed layers 1, 4	0.01	0.04	0.01	0.01	**0.04**

Table 5.1: Systematic uncertainty assigned for each analysis option, detailed in appendix C.

The uncertainty in each mean of residuals was assigned as the sum in quadrature of the statistical uncertainty in the mean and the appropriate systematic uncertainty for the tracking combination.

5.8 Discussion

Cosmics data is being used to calculate relative alignment parameters using two other methods [60]. A cross-check of this analysis would be to compare their results; however the studies in appendix C show that the mean cosmics residuals are robust, so the comparison was not prioritized.

Given that the uncertainty in the residual means is lesser than or near to the order of the required position resolution of the sTGCs (100 µm [5]) they are relevant input for alignment studies.

The relative local offsets as calculated from the mean of residual distributions provide a complete picture of the relative alignment between detectors planes. In fact, cosmic muon testing is the only characterization technique where the entire surface of quadruplet layers can be probed since muons hits are distributed almost uniformly; the CMM [7] and x-ray methods [8] depend on measurements at reference points, and test beams only have a limited beam spot [6]. By looking at 2D-histograms of residual means like figure 5.6 for all tracking combinations, it is easy to identify quadruplets that suffer large relative misalignment since many residual means differ significantly from zero. Moreover, the pattern in the relative local offsets can be used to motivate a physical interpretation of misalignments. The relative local offsets can be used as a reference, cross check, or input in other alignment studies.

Relative local offsets cannot be used to position strips in the absolute ATLAS coordinate system because there was no external reference to measure positions on all layers with respect to. The lack of external reference means that there is not enough information to unfold relative local offsets into absolute local offsets (with respect to the nominal quadruplet geometry). As an example, assuming that the residual on layer 2 in figure 5.4 is representative of the relative local offset, the residual on layer 2 could be caused by the strips on layer 2 being misaligned from nominal, but it could also be caused by strips on layers 1 and 4 being offset from nominal while the strips on layer 2 are in their nominal positions! Any number of combinations of local offsets on layers 1, 2 and 4 could produce the residual on layer 2. Absolute local offsets must be calculated another way.

Chapter 6

Using x-rays to measure relative strip position offsets

Local offset measurements were done with the x-ray method. The reader is referred to the paper describing the x-ray method [8], although some minor changes have been made to the experimental setup since it was written. The experimental setup described here is current and was used to collect the data presented in this thesis.

6.1 Experimental setup

The x-ray tests were performed after the quadruplets arrived at CERN, were assembled into wedges, and alignment platforms installed. Essentially, an x-ray gun was attached to one of the alignment platforms glued to the surface of the wedge and the x-ray beam profile recorded by the strips.

The wedges were installed on carts that could rotate their surface to a horizontal position. A mounting platform was installed on top of the alignment platform using a three-ball mount. The x-ray gun used was an Amptek Mini-X tube. The gun was placed in a brass holder with built-in 2 mm collimator and 280 µm copper filter. The holder was mounted on one of five positions on the mounting platform, as shown in figure 6.1. Gun positions were chosen to avoid wire support structures in the sTGCs that reduce hit efficiency [60] and boundaries between sets of strips read out by two different ASICs that could each have different thresholds.

As with cosmics data collection, each sTGC also needed gas and high voltage to operate.

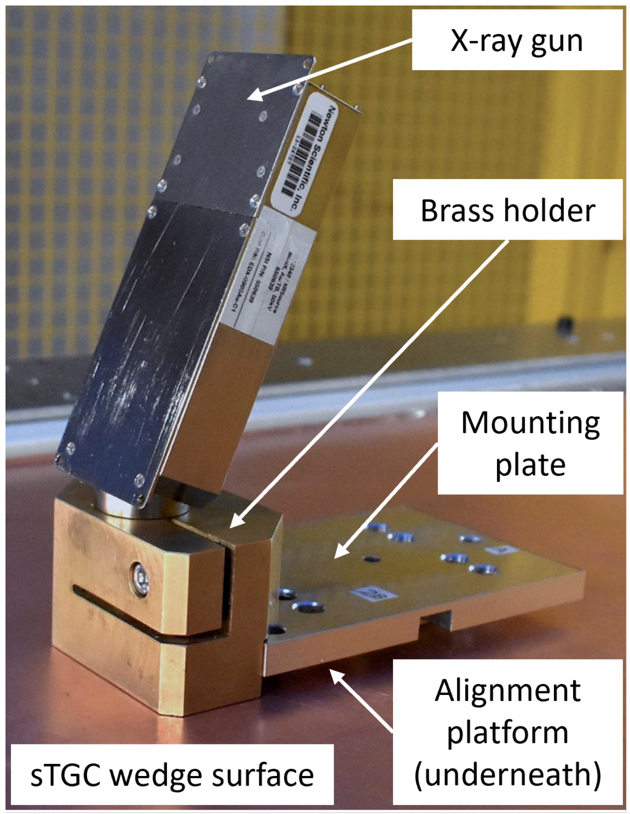

Figure 6.1: The x-ray gun mounted to the alignment platform on the surface of the wedge. Adapted from [8].

Each layer was operated at 2.925 kV with high voltage from a NIM crate. The chambers were flushed with CO_2 before and during data collection.

The gun produced x-rays with energies under 40 keV with peaks in the 7-15 keV range. The x-rays mostly interacted with the wedge's copper electrodes and gold-plated tungsten wires via the photo effect. The resulting photoelectrons caused ionization avalanches that were picked up by the strips.

6.2 Data acquisition

A different version of the same front end electronics, but the same ASIC, as used in cosmics testing were used for the x-ray testing to amplify the data and measure the peak signal amplitude. Data was collected for two minutes per gun position with random triggers. A trigger recorded all signals above threshold. Pad and wire data was not recorded.

6.3 Data preparation

Like with cosmics analysis, a default pedestal is subtracted from the signal peak amplitude on each electrode.

Clusters are defined as groups of contiguous strip hits collected within 75 ns. The peak signal amplitude of each electrode in a cluster is fit with a Gaussian, and the mean of the Gaussian is taken as the cluster position. Cluster positions are corrected for DNL (see definition in appendix C.4). Only clusters composed of hits on 3-5 strips were used in the x-ray analysis. Clusters with signal on more than 5 strips were cut because they were most likely caused by photoelectrons ejected with enough energy to be δ-rays.

The x-ray analysis diverges entirely from the cosmics analysis algorithm here because the x-rays do not leave tracks. The signals picked up by the strips are from photoelectrons liberated from the metals of the sTGCs, which only travel through one gas volume and are ejected at all angles. Instead of creating tracks, the cluster position distribution on each layer is used to define the beam profile. A typical beam profile is shown in figure 6.2.

6.4 Measuring local offsets

The mean of the cluster position distribution is taken as the x-ray beam profile center. The expected center is calculated assuming a wedge with nominal geometry given the gun

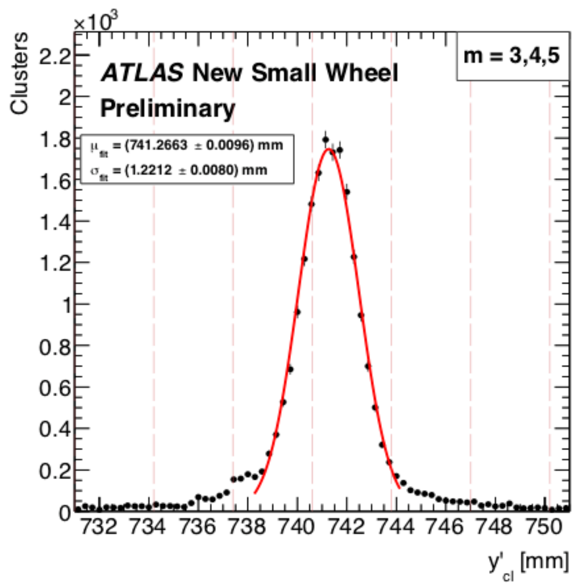

Figure 6.2: Distribution of x-ray cluster mean positions after the analysis cuts and corrections. The strip cluster multiplicity, m, was limited to 3, 4 and 5. The red curve is a Gaussian fit of the distribution and the pink dashed lines denote the edges of the strips [8].

position, corrected for: the geometry of the brass holder, the positioning and angle of the alignment platforms and the beam angle. The difference between the expected and reconstructed beam profile center is a measure of the local offset. Applying the logic of equation 5.1 to the beam profile, the Gaussian mean of cluster positions on the given layer acts as the recorded position, y_i, the expected center is $y_{nom,i}$ and the local offset is $d_{local,i}$ as before, where i denotes the layer. Since the position of the alignment platforms will be monitored by the alignment system in ATLAS [5], the position of the strips that should have been at he gun position are shifted by $d_{local,i}$ and so are known in the ATLAS coordinate system for every position where x-ray data was taken.

The x-ray working group accepted an uncertainty of 120 µm on the beam profile centers. The largest uncertainty comes from the effect of the gun angle, which proved difficult to measure and correct for.

The local offsets are not presented here as the author did not conduct this work. However, the author used the local offsets to calculate relative local offsets.

6.5 Measuring relative local offsets

The x-ray local offsets were shown to be correlated with the local offsets calculated from the CMM data, but the CMM data does not include the effect of inter-layer misalignments so the degree of correlation measurable was limited. Cosmics data is affected by inter-layer misalignments. Since the local offsets for x-rays and cosmics data are measured in different coordinate systems, they cannot be compared directly. Bringing the cosmics relative local offsets into an absolute coordinate system is impossible; however, the x-ray local offsets can be brought into a relative coordinate system.

The measured x-ray beam profile centers were systematically affected by local offsets in the same way as the mean cosmics residuals, as modeled by equation 5.1. Therefore, if a 2-layer track is built from the beam profile centers on each layer and the residual calculated on a third layer, that residual should match the local mean cosmics residual. The residual is the difference between the beam profile center on the layer of interest and the polated track position from the beam profile centers recorded on the two fixed layers. The beam profile center on the layer of interest acts as y_i and the polated track position acts as $y_{track,i}$ in equation 5.2.

The built track is not an actual track of the x-ray beam. A beam profile center is actually the Gaussian mean of all selected mean cluster positions recorded during the x-ray data taking period, not a single hit of a track. Building an "abstract" track was necessary because the x-rays cause signal in the chamber via the photoeffect so there were not individual "x-ray tracks" to record. In fact the x-ray data could be collected separately for each layer. Nonetheless, since the effect of local offsets on the beam profile centers was the same as their effect on the recorded cosmics cluster positions the difference in algorithm between x-ray and cosmics analysis was allowed.

For each x-ray survey position, the x-ray residual was calculated for all possible tracking combinations (which required an x-ray beam profile on at least three layers). The x-ray residuals on layer 2 calculated from the beam profile centers recorded on layers 1 and 3 are represented as arrows in figure 6.3 as arrows for QL2.P.11 and QL2.P.8. For QL2.P.11, a negative offset at all x-ray survey positions is clear.

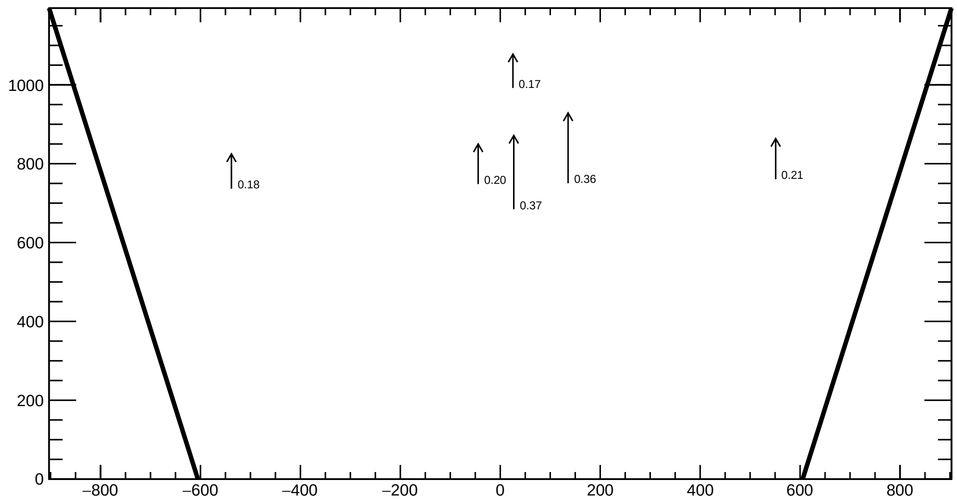

(a) QL2.P.11 x-ray residuals on layer 2, reference layers 1 and 3.

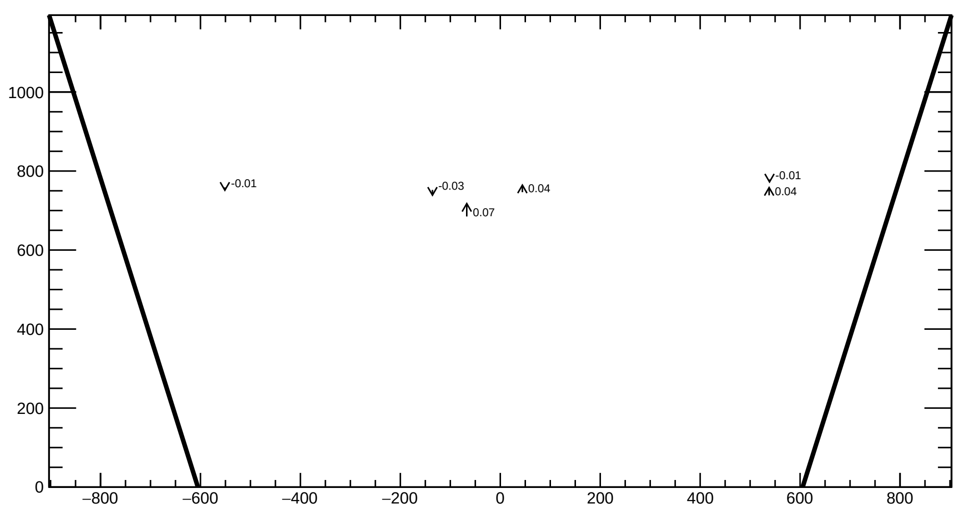

(b) QL2.P.8 x-ray residuals on layer 2, reference layers 1 and 3.

Figure 6.3: The x-ray residuals on layer 2 calculated from the beam profile centers recorded on layers 1 and 3 for QL2.P.11 and QL2.P.8. The arrows originate from the expected position of the beam profile center assuming a nominal geometry, and the lengths are proportional to the calculated x-ray residuals. The tip of the arrow represents where the recorded hit was with respect to where it should have been recorded nominally. The value of the x-ray residuals are annotated in millimeters and have an uncertainty of $\pm 0.15\,\mathrm{mm}$.

The uncertainty on the x-ray residuals was the error propagated through the tracking, taking an uncertainty of 120 µm on each beam profile center. The uncertainty on the x-ray residuals ranged from 0.15 mm to 0.4 mm from the most to least geometrically-favourable tracking combination. There is no discernible pattern to the x-ray residuals on QL2.P.8 because they are smaller than the uncertainty. The x-ray residual uncertainties are significantly larger than the uncertainties on the relative local offsets calculated with cosmics data.

Chapter 7

Comparing cosmic muon and x-ray relative strip position offsets

The goal was to validate the local offsets extracted from the x-ray data with cosmics data. The complication was that the x-ray dataset provided absolute local offsets while the cosmics dataset provided relative local offsets, which could not be compared directly. The solution was to use the x-ray local offsets to calculate relative local offsets. The x-ray relative local offset is the x-ray residual reconstructed from an abstract track using the beam profile centers on each layer as the track hits. The cosmics relative local offset was taken as the Gaussian mean of muon track residuals in a 100 mm by 100 mm area, referred to the as the mean cosmics residual. Relative local offsets of each type calculated using the same reference layers are compared for each area where x-ray data is available. The results of the comparison are presented here.

7.1 Assessing correlation

The 2D visualizations of the mean cosmics and x-ray residuals for tracks on layer 2 with reference layers 1 and 3 on QL2.P.11 and QL2.P.8 are shown in figure 7.1. Figure 7.1 is a superposition of figures 5.6 and 6.3.

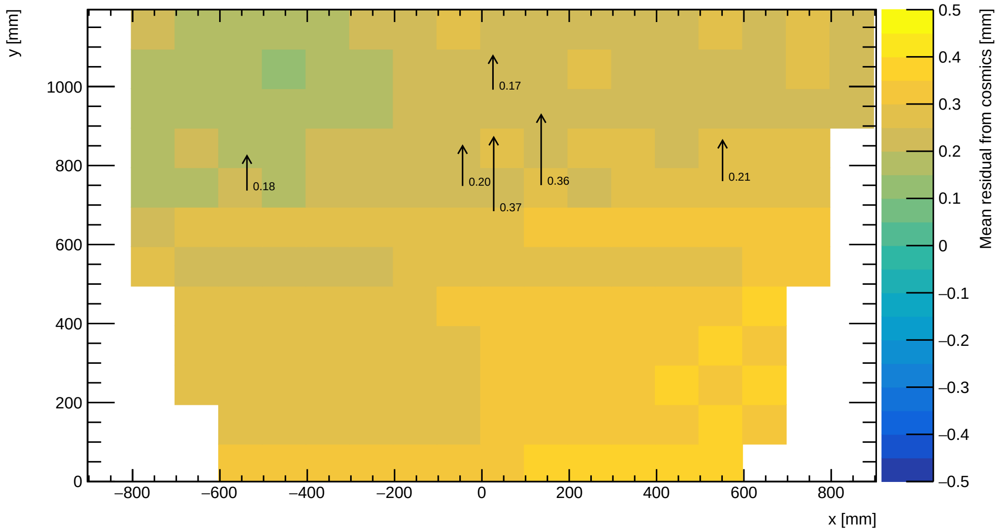

(a) QL2.P.11 residuals of tracks on layer 2, reference layers 1 and 3.

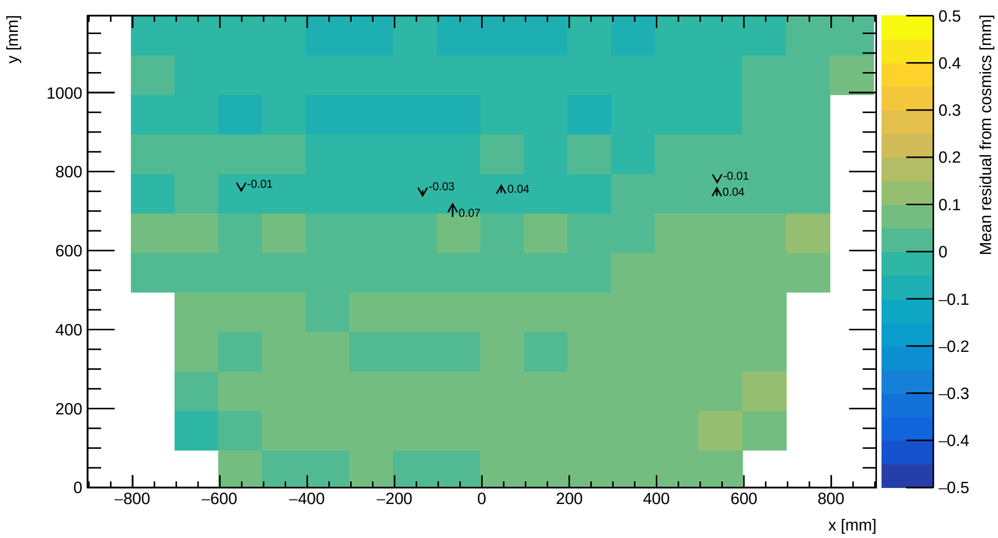

(b) QL2.P.8 residuals of tracks on layer 2, reference layers 1 and 3.

Figure 7.1: The mean cosmics residuals are shown using colour. The x-ray residuals available at nominal gun positions are drawn as arrows and the value of the residual annotated in millimeters with uncertainty ± 0.15 mm. The length of the arrows is 500 times the value of the x-ray residual, scaled for visibility. These plots are a superposition of figures 5.6 and 6.3.

Figure 7.1a shows that for QL2.P.11 the x-ray residuals are of the same sign and order as the mean cosmics residuals, as can be seen by comparing the the annotated value of the x-ray residual to the mean cosmics residual represented by colour; QL2.P.11's mean cosmics and x-ray residuals are correlated to some degree. For QL2.P.8, the x-ray residuals are of the right order compared to the mean cosmics residuals, but the correlation is less apparent. While x-ray residuals do not reveal a pattern across the layer's surface, the mean cosmics residuals show a structure to the relative local offsets since they vary smoothly over the surface of layer 2.

The comparison of mean cosmics and x-ray residuals was done for several quadruplets for all tracking combinations (not just layer 2 residuals calculated with fixed layers 1 and 3 like in figure 7.1). Scatter plots of the x-ray and mean cosmics residuals on QL2.P.11 and -2 for all tracking combinations shown in figures 7.2 and 7.3 reveal the degree of correlation between the datasets. In the correlation plots, each rectangle is centered on the value of a mean cosmics and x-ray residual pair calculated with a given tracking combination for every gun position where data is available; the height and width of the squares are the uncertainty in the mean cosmics and x-ray residuals respectively. Note that in the scatter plots, the regions of interest where cosmics tracks are included in the calculation of mean of residuals are exactly centered on the nominal x-ray beam position, unlike in figure 7.1.

The fitted slope and offset in figure 7.2 show that the two QL2.P.11 datasets are correlated. The large uncertainty on the x-ray residuals set a limit on the sensitivity of the analysis, for if the absolute value of the x-ray residuals of a quadruplet were smaller than the x-ray residual uncertainties, no conclusion about the correlation could be drawn, like for QL2.P.8 (figure 7.3). This result is reflected in the small x-ray residuals shown in figure 7.1b that do not reveal a pattern in the relative local offsets across the surface of layer 2. However, figure 7.3 shows that the x-ray and mean cosmics residuals are centered around zero, as is expected for a quadruplet with small relative misalignments between layers.

There are three patterns in the residuals on the scatter plot explained by geometry. First, for both datasets the uncertainty in the extrapolated track residuals were larger than the interpolated track residuals because of the extrapolation lever arm. For the x-ray residuals, the effect of the lever arm on the uncertainty was direct since the residual was calculated from a single abstract track; for the mean cosmics residuals it was the widening of the residual distribution due to the extrapolation lever arm that increased the uncertainty in the fitted mean of residuals. Second, residuals calculated through extrapolation tend to be larger because the extrapolation lever arm can produce more extreme values of the track position on the layer of interest. Third, the points in figure 7.2 are geometrically correlated (e.g. they seem to be roughly mirrored around the origin). This is expected since the residuals calculated using a given set of three layers should be geometrically correlated by the local

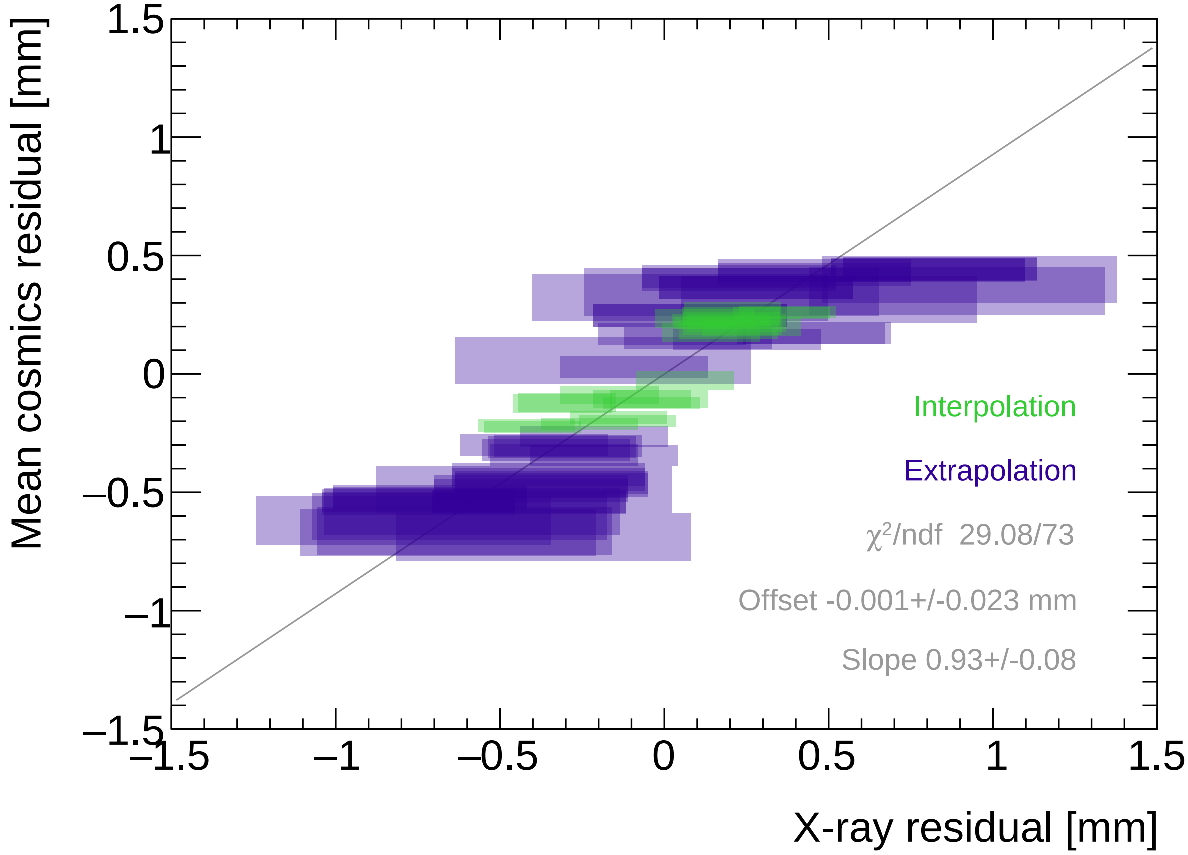

Figure 7.2: Correlation plot between x-ray and mean cosmics residuals for all tracking combinations for QL2.P.11. Each rectangle is centered on an x-ray and mean cosmics residual pair calculated at a given gun position and for a certain tracking combination. The width of the rectangles in x and y are the uncertainty in the x-ray and mean cosmics residual respectively. A printer-friendly version of this plot is available in appendix D.

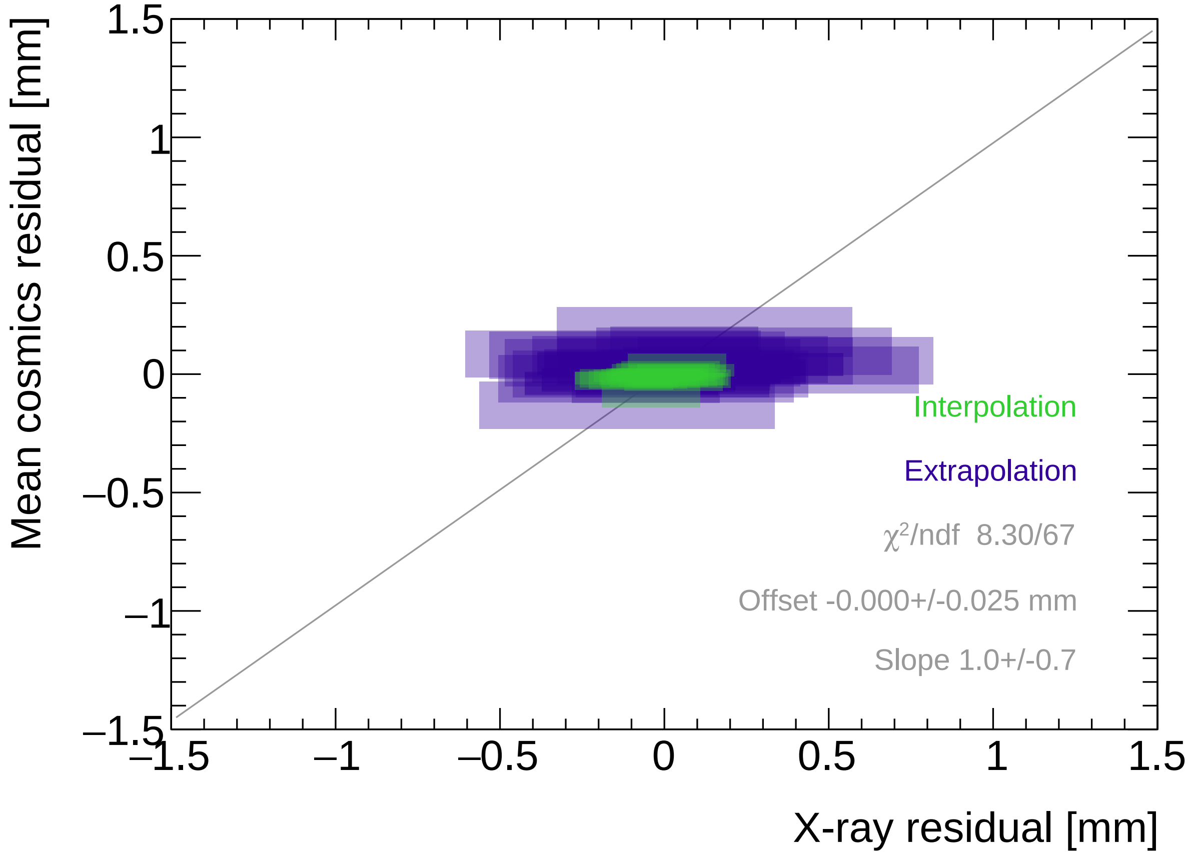

Figure 7.3: Correlation plot between x-ray and mean cosmics residuals for all tracking combinations for quadruplet 2. Each rectangle is centered on an x-ray and mean cosmics residual pair calculated at a given gun position and for a certain tracking combination. The width of the rectangles in x and y are the uncertainty in the x-ray and mean cosmics residual respectively. A printer-friendly version of this plot is available in appendix D.

offsets on the fixed layers and the layer of interest (the $d_{local,i}$ on each layer as defined in equation 5.1).

7.2 Discussion

Several quadruplets were tested for each quadruplet construction geometry built in Canada. Each quadruplet fell into one of the two categories: residuals large enough to see a correlation, or residuals too small to see a correlation. Since the x-ray and mean cosmics residuals were measures of the relative local offsets between the layer and the two reference layers, quadruplets with the largest relative misalignments had the largest range of residuals. the correlation plots were an easy visual way to identify quadruplets with large relative misalignments.

The most significant limit on measuring the degree of correlation between the x-ray and mean cosmics residuals was the uncertainty on the x-ray residuals, which stemmed from the systematic uncertainty of 120 µm in the x-ray beam profile centers used to build the abtract tracks. For example, in figure 7.3 the uncertainty in the x-ray residuals makes detecting correlation impossible. The x-ray method was limited primarily by the systematic uncertainties in the relative alignment of the platforms and the gun, especially the gun angle.

The analysis of certain quadruplets was limited by the availability of data. Sometimes, less than three layers were surveyed for a given x-ray gun position so no residuals could be calculated. Too few x-ray residuals prevented the analysis from detecting a significant correlation, should it even be measurable. Often, the analysis of smaller quadruplets (placed innermost on the wheel) suffered as a result because they had fewer alignment platforms, and hence gun positions, on their surfaces. The analysis was also limited to certain quadruplets. The wedges constructed the earliest (typically small wedges) were surveyed when the x-ray method was still being designed and so have limited x-ray residuals calculated from beam profiles of lower quality. In addition, not all cosmic muon test sites had enough front end electronics to collect data on three layers simultaneously, which is the minimum required to be able to calculate residuals.

Nonetheless, the comparison of x-ray and cosmics residuals was really to confirm the x-ray method's ability to measure local offsets with an independent dataset. The x-ray local offsets allow the calculation of relative local offsets that have been correlated to the cosmics relative local offsets. Therefore, the analysis of quadruplets with relative local offsets large enough to detect a correlation validates the x-ray method's ability to measure local offsets.

The potential of using relative local offsets calculated from cosmics data to study relative alignment between sTGC layers stands on its own. For example, although the x-ray relative local offsets of QL2.P.8 in figure 7.1b do not reveal a pattern, the variation in the cosmics relative local offsets do. Identifying the pattern is possible because mean cosmics residuals can be calculated across the entire area and are sensitive to smaller relative local offsets since their uncertainty is significantly smaller.

The advantage of the x-ray dataset over the cosmics dataset is that absolute local offsets are measurable thanks to the reference frame provided by the alignment platforms. This is required to measure the position of strips in the ATLAS coordinate system to satisfy the NSWs' precision tracking goals. The x-ray local offsets are being used to build an alignment model of strips in each quadruplet. It is compelling to imagine using the cosmics relative local offsets to improve the model considering their precision and ability to capture effects across the entire area of the quadruplet.

Chapter 8

Outlook and summary

The cosmic muon dataset was used to independently confirm the absolute local offsets measured by the x-ray method. The x-ray offsets are being used to complete the sTGC alignment scheme of the NSWs: the NSW alignment system monitors the position of alignment platforms on the surface of sTGC wedges, and the x-ray measurements provide the offsets of the strip pattern with respect to each alignment platform. The continuation of this analysis is detailed next (section 8.1) before summarizing and considering the larger context (section 8.2).

8.1 Outlook

Next all quadruplets with suitable cosmics and x-ray data should be surveyed to flag anomalous quadruplets (as a first step). If a quadruplet's correlation plot like figure 7.2 or 7.3 reveals an unexpected correlation or has a large scatter, it would indicate an issue with either the cosmics or x-ray data collection to be investigated further. The uncertainty in each set of tracking points would inform the interpretation of the anomaly. Then, the quality of the correlation should be evaluated over all quadruplets instead of individually.

For now, the correlation for the individual quadruplets tested support the use of the x-ray data to build an alignment model [8]. Work on creating an alignment model is ongoing. Currently, the algorithm compares the y-position of a local group of strips at each x-ray gun position as measured by the x-ray and CMM methods in a fit to extract a global slope (m)

and offset (b) per layer, i, where the χ^2 is given by equation 8.1.

$$\chi^2 = \frac{\left[dy_{cmm,corr} - dy_{xray}\right]^2}{\delta dy_{xray}^2 + \delta dy_{cmm,corr}^2}\,, \tag{8.1}$$

$$dy_{cmm,corr} = y_{cmm} + b_i + m_i x - y_{nom} \tag{8.2}$$

Here, dy refers to the corrected CMM and x-ray local offsets, and δdy refers to their respective uncertainties. The CMM measurements were taken before the cathode boards were assembled into quadruplets, so alignment parameters for the given layer were extracted from the χ^2 fit by stepping the corrected CMM y-position towards the x-ray y-position by adjusting the layer's slope and offset parameters. The plan is that the alignment parameters will be provided to the ATLAS experiment's offline software to reconstruct muon tracks from the NSWs' sTGCs. The large uncertainty on the x-ray local offsets (120 µm) and the sparseness of the measurements means that including input from other characterization datasets could reduce the uncertainty on the alignment model parameters.

The uncertainty in the mean cosmics residuals was smaller than the desired position resolution of the sTGCs, so they provide relevant information about strip positions. Moreover, they can be calculated over the entire area of the quadruplet instead of at specific positions. It would be great to use the cosmics residuals as input to calculate and reduce the uncertainty on the alignment parameters. Since mean cosmics residuals can only provide relative alignment information, one idea would be to use them to constrain the fit of the alignment parameters. In this case, the alignment parameters would need to be fitted on all layers at once, and the shifting y-positions on each layer forced to create an abstracted track residual equal to the local mean cosmics residual (within uncertainty) for each x-ray point. Or, instead of constraining the fit, it could be penalized if the resulting parameters do not result in abstracted track residuals equal to the mean cosmics residuals within uncertainty. Some work on using the three datasets at once in a fit has been started.

8.2 Summary

The LHC [1] will be at the energy frontier of particle physics for at least the next decade, making it a unique tool with which to study particle physics. With the HL-LHC [2], high statistics on rare particle physics processes will enable more precise measurements of parameters of the Standard Model and increase the sensitivity to signatures of physics beyond the Standard Model [3]. To capitalize on the increased collision rate, the NSWs of the ATLAS experiment must be replaced to keep the triggering and tracking performance [5].

Small-strip thin gap chambers are gas ionization chambers optimized for a high rate environment [5]. Using the pad electrodes to define a region of interest makes it possible to get track segments of ∼1 mrad angular resolution quickly, which will be used as input to check if a collision originated from the interaction point and should be triggered on or not [5, 54]. sTGCs are also able to provide better than 100 µm position resolution on each detector plane to fulfill precision offline tracking requirements [6].

Ultimately, the positions of the sTGC strip electrodes need to be known in ATLAS to within ∼100 µm so that they can deliver the required position resolution. The ATLAS alignment system will position alignment platforms on the surface of the sTGC wedge, and an alignment model will be used to position the strips with respect to the alignment platforms [5]. Input to the alignment model comes from the datasets used to characterize the quadruplets. The x-ray method [8] is used to measure offsets of strips from their nominal position to achieve this goal. The alignment model could be built on x-ray data alone, but the sparseness of and large uncertainty on the local offsets mean that the alignment model could benefit from more input. Comparing the x-ray offsets to the CMM data [7] allows the effect of inter-layer misalignments to be isolated and increases the input to the alignment model.

The cosmics dataset was used to confirm the local offsets measured with the x-ray gun. It provides relative local offsets between sTGC strip layers. The 2D visualizations of relative local offsets allow personnel to quickly identify areas of misaligned strips and make hypotheses of the physical origin of those misalignments. The correlation seen between the x-ray and cosmics relative local offsets in quadruplets with large relative misalignments both confirms the validity of the x-ray local offsets and again is a quick way to identify quadruplets with large misalignments. Moreover, the mean of track residuals in an area is a robust estimation of the relative local offset, as shown by the estimation of systematic uncertainties; the relative local offsets for all two-fixed layer reference frames do not change by more than 100 µm given variation in data collection conditions and analysis algorithms. The cosmics relative local offsets are therefore relevant input for alignment studies and could improve the alignment model that will position each strip.

Achieving the required position resolution on each layer of the NSWs in the particle track bending plane achieves the design momentum resolution for muons ejected towards the endcaps of ATLAS. Muons are important signatures of electroweak and Higgs sector events of interest for the ATLAS Collaboration's future physics goals [5]. Being the second of two tracking technologies on the NSWs, an effective alignment model of sTGC quadruplets layers is a necessary part of making the NSWs redundant for 10 or more years of recording collisions in the High Luminosity era of the LHC.

References

[1] L Evans and P Bryant. LHC Machine. *Journal of Instrumentation*, 3(S08001), 2008.

[2] G Apollinari, I Bejar Alonso, O Bruning, P Fessia, M Lamont, L Rossi, and L Tavian. High-Luminosity Large Hadron Collider (HL-LHC) Technical Design Report V. 0.1. Technical report, CERN, Geneva, September 2017.

[3] A Dainese et al. The physics potential of HL-LHC. In *Input to the European Particle Physics Strategy Update*, November 2018.

[4] The ATLAS Collaboration. The ATLAS Experiment at the CERN Large Hadron Collider. *Journal of Instrumentation*, 3(08):S08003, 2008.

[5] T Kawamoto, S Vlachos, L Pontecorvo, J Dubbert, G Mikenberg, P Iengo, C Dallapiccola, C Amelung, L Levinson, R Richter, and D Lellouch. New Small Wheel Technical Design Report. Technical report, Jun 2013. ATLAS New Small Wheel Technical Design Report.

[6] Angel Abusleme et al. Performance of a Full-Size Small-Strip Thin Gap Chamber Prototype for the ATLAS New Small Wheel Muon Upgrade. *Nuclear Instruments and Methods in Physics Research Section A: Accelerators, Spectrometers, Detectors and Associated Equipment*, 817:85–92, May 2016. arXiv: 1509.06329.

[7] Evan Michael Carlson. *Results of the 2018 ATLAS sTGC test beam and internal strip alignment of sTGC detectors*. Thesis, University of Victoria, Victoria, Canada, 2019. Accepted: 2019-07-16T17:20:40Z.

[8] B. Lefebvre. Precision survey of the readout strips of small-strip Thin Gap Chambers using X-rays for the muon spectrometer upgrade of the ATLAS experiment. *Journal of Instrumentation*, 15(07):C07013–C07013, July 2020.

[9] David J. Griffiths. *Introduction to elementary particles*. Physics textbook. Wiley-VCH, Weinheim, Germany, 2., rev. ed., 5. reprint edition, 2011.

[10] Michael Edward Peskin and Daniel V. Schroeder. *An introduction to quantum field theory*. Addison-Wesley Pub. Co, Reading, Massachusetts, 1995.

[11] P.A. Zyla et al. Review of Particle Physics. *PTEP*, 2020(8):083C01, 2020.

[12] Makoto Kobayashi and Toshihide Maskawa. CP-violation in the renormalizable theory of weak interaction. *Progress of theoretical physics*, 49(2):652–657, February 1973.

[13] M. L. Perl, G. S. Abrams, A. M. Boyarski, M. Breidenbach, D. D. Briggs, F. Bulos, W. Chinowsky, J. T. Dakin, G. J. Feldman, C. E. Friedberg, D. Fryberger, G. Goldhaber, G. Hanson, F. B. Heile, B. Jean-Marie, J. A. Kadyk, R. R. Larsen, A. M. Litke, D. Lüke, B. A. Lulu, V. Lüth, D. Lyon, C. C. Morehouse, J. M. Paterson, F. M. Pierre, T. P. Pun, P. A. Rapidis, B. Richter, B. Sadoulet, R. F. Schwitters, W. Tanenbaum, G. H. Trilling, F. Vannucci, J. S. Whitaker, F. C. Winkelmann, and J. E. Wiss. Evidence for Anomalous Lepton Production in ${e}ˆ{+}\ensuremath{-}{e}ˆ{\ensuremath{-}}$ Annihilation. *Physical Review Letters*, 35(22):1489–1492, December 1975. Publisher: American Physical Society.

[14] F. Englert and R. Brout. Broken Symmetry and the Mass of Gauge Vector Mesons. *Physical Review Letters*, 13(9):321–323, August 1964. Publisher: American Physical Society.

[15] P. W. Higgs. Broken symmetries, massless particles and gauge fields. *Physics Letters*, 12(2):132–133, September 1964.

[16] David Galbraith and Carsten Burgard. UX: Standard Model of the Standard Model, November 2013.

[17] Carlos A. Bertulani. *Nuclear physics in a nutshell*. In a nutshell. Princeton University Press, Princeton, N.J, 2007. OCLC: ocm85690422.

[18] Bradley W. Carroll and Dale A. Ostlie. *An introduction to modern astrophysics*. Pearson Addison-Wesley, San Francisco, 2nd ed edition, 2007. OCLC: ocm69020924.

[19] Mirko Boezio and Emiliano Mocchiutti. Chemical composition of galactic cosmic rays with space experiments. *Astroparticle Physics*, 39-40:95–108, December 2012.

[20] B. Aharmim et al. Combined analysis of all three phases of solar neutrino data from the sudbury neutrino observatory. *Phys. Rev. C*, 88:025501, Aug 2013.

[21] B. Pontecorvo. Neutrino Experiments and the Problem of Conservation of Leptonic Charge. *Zh. Eksp. Teor. Fiz.*, 53:1717–1725, 1967.

[22] S. M. Bilenky and S. T. Petcov. Massive neutrinos and neutrino oscillations. *Reviews of Modern Physics*, 59(3):671–754, July 1987.

[23] Bing-Lin Young. A survey of dark matter and related topics in cosmology. *Frontiers of Physics*, 12(2):121201, April 2017.

[24] Carlos Muñoz. Dark matter detection in the light of recent experimental results. *International Journal of Modern Physics A*, 19(19):3093–3169, July 2004.

[25] Gerard Jungman, Marc Kamionkowski, and Kim Griest. Supersymmetric dark matter. *Physics Reports*, 267(5):195–373, March 1996.

[26] G. Arnison et al. Experimental observation of isolated large transverse energy electrons with associated missing energy at s=540 GeV. *Physics Letters B*, 122(1):103–116, February 1983.

[27] M. Banner et al. Observation of single isolated electrons of high transverse momentum in events with missing transverse energy at the CERN pp collider. *Physics Letters B*, 122(5):476–485, March 1983.

[28] G. Arnison et al. Experimental observation of lepton pairs of invariant mass around 95 GeV/c2 at the CERN SPS collider. *Physics Letters B*, 126(5):398–410, July 1983.

[29] P. Bagnaia et al. Evidence for Z→ e^+e^- at the CERN pp collider. *Physics Letters B*, 129(1):130–140, 1983.

[30] CDF Collaboration. Observation of Top Quark Production in $\overline{\mathit{p}}\mathit{p}$ Collisions with the Collider Detector at Fermilab. *Physical Review Letters*, 74(14):2626–2631, April 1995. Publisher: American Physical Society.

[31] D0 Collaboration. Observation of the Top Quark. *Physical Review Letters*, 74(14):2632–2637, April 1995. Publisher: American Physical Society.

[32] The ATLAS Collaboration. Observation of a new particle in the search for the Standard Model Higgs boson with the ATLAS detector at the LHC. *Physics Letters B*, 716(1):1–29, September 2012. arXiv: 1207.7214.

[33] The CMS Collaboration. Observation of a new boson at a mass of 125 GeV with the CMS experiment at the LHC. *Physics Letters B*, 716(1):30–61, September 2012. arXiv: 1207.7235.

[34] Standard Model Summary Plots June 2021.

[35] Oliver Sim Brüning, Paul Collier, P Lebrun, Stephen Myers, Ranko Ostojic, John Poole, and Paul Proudlock. *LHC Design Report*. CERN Yellow Reports: Monographs. Geneva, 2004.

[36] ATLAS luminosity public results run-1, March 2011.

[37] ATLAS luminosity public results run-2, July 2015.

[38] The European Strategy for Particle Physics. Technical Report CERN/2685, CERN, 2006. Adopted by the CERN council at a special session at ministerial level in Lisbon in 2006.

[39] HiLumi HL-LHC Project. LHC/HL-LHC plan (last update january 2021). https://hilumilhc.web.cern.ch/content/hl-lhc-project, last accessed on 2021-09-09.

[40] M. Cepeda et al. Report from Working Group 2: Higgs Physics at the HL-LHC and HE-LHC. *CERN Yellow Rep. Monogr.*, 7:221–584. 364 p, Dec 2018.

[41] ATLAS inner detector : Technical Design Report, 1. Technical Report CERN-LHCC-97-016, CERN, 1997. ISBN: 9789290831020 Publication Title: CERN Document Server.

[42] L. Rossi, S. Haywood, A. Romaniouk, and R. Nickerson. ATLAS inner detector : Technical Design Report, 2. Technical Report CERN-LHCC-97-017, CERN, 1997. ISBN: 9789290831037 Publication Title: CERN Document Server.

[43] Claus Grupen, Boris A Shwartz, and Helmuth Spieler. *Particle detectors*. Cambridge University Press, Cambridge, UK; New York, 2008. OCLC: 1105536566.

[44] ATLAS liquid-argon calorimeter : Technical Design Report. Technical Report CERN-LHCC-96-041, CERN, 1996. ISBN: 9789290830900 Publication Title: CERN Document Server.

[45] ATLAS tile calorimeter : Technical Design Report. Technical Report CERN-LHCC-96-042, CERN, 1996. ISBN: 9789290830917 Publication Title: CERN Document Server.

[46] ATLAS Collaboration. ATLAS Muon Spectrometer: Technical Design Report. Technical Report CERN-LHCC-97-022, CERN, Geneva, 1997.

[47] ATLAS magnet system : Technical Design Report, 1. Technical Report CERN-LHCC-97-018, CERN, 1997. ISBN: 9789290831044 Publication Title: CERN Document Server.

[48] ATLAS Collaboration. Performance of the ATLAS muon trigger in pp collisions at $\sqrt{s}=8$ TeV. *The European Physical Journal C*, 75(3):120, March 2015. arXiv: 1408.3179.

[49] S. Aefsky, C. Amelung, J. Bensinger, C. Blocker, A. Dushkin, M. Gardner, K. Hashemi, E. Henry, B. Kaplan, P. Keselman, M. Ketchum, U. Landgraf, A. Ostapchuk, J. Rothberg, A. Schricker, N. Skvorodnev, and H. Wellenstein. The Optical Alignment System of the ATLAS Muon Spectrometer Endcaps. *Journal of Instrumentation*, 3(11):P11005–P11005, November 2008. Publisher: IOP Publishing.

[50] ATLAS level-1 trigger : Technical Design Report. Technical Report CERN-LHCC-98-014, CERN, 1998. ISBN: 9789290831280 Publication Title: CERN Document Server.

[51] A Ruiz Martínez and. The run-2 ATLAS trigger system. *Journal of Physics: Conference Series*, 762:012003, oct 2016.

[52] Technical Design Report for the Phase-II Upgrade of the ATLAS TDAQ System. Technical report, CERN, Geneva, Sep 2017.

[53] Marzio Nessi, Markus Nordberg, Peter Jenni, and Kenway Smith. ATLAS high-level trigger, data-acquisition and controls : Technical Design Report. Technical Report CERN-LHCC-2003-022, CERN, 2003. Publication Title: CERN Document Server.

[54] E. Perez Codina. Small-strip Thin Gap Chambers for the muon spectrometer upgrade of the ATLAS experiment. *Nuclear Instruments and Methods in Physics Research Section A: Accelerators, Spectrometers, Detectors and Associated Equipment*, 824:559–561, July 2016.

[55] John Townsend. *Electricity in gases*. Clarendon Press, Oxford, 1915.

[56] S. Majewski, G. Charpak, A. Breskin, and G. Mikenberg. A thin multiwire chamber operating in the high multiplication mode. *Nuclear Instruments and Methods*, 217:265–271, 1983.

[57] E. Gatti, A. Longoni, H. Okuno, and P. Semenza. Optimum geometry for strip cathodes or grids in MWPC for avalanche localization along the anode wires. *Nuclear Instruments and Methods*, 163(1):83–92, July 1979.

[58] G. Battistoni, P. Campana, V. Chiarella, U. Denni, E. Iarocci, and G. Nicoletti. Resistive cathode transparency. *Nuclear Instruments and Methods in Physics Research*, 202(3):459–464, November 1982.

[59] P. K. F. Grieder. *Cosmic rays at Earth: researcher's reference manual and data book*. Elsevier Science Ltd, Amsterdam, 1st ed edition, 2001.

[60] Benoit Lefebvre. *Characterization studies of small-strip Thin Gap Chambers for the ATLAS Upgrade*. PhD Dissertation, McGill University, Montreal, Canada, 2018.

[61] R. Keyes, K.A. Johnson, L. Pepin, F. Léger, C. Qin, S. Webster, A. Robichaud-Véronneau, C. Bélanger-Champagne, B. Lefebvre, S.H. Robertson, A. Warburton, B. Vachon, and F. Corriveau. Development and characterization of a gas system and its associated slow-control system for an ATLAS small-strip thin gap chamber testing facility. *Journal of Instrumentation*, 12(04):P04027–P04027, April 2017.

[62] George Iakovidis. VMM3, an ASIC for Micropattern Detectors. In *Proceedings of Science*, page 5, Philadelphia, 2017.

[63] Bohan Chen. *Calibration Studies of the Front-End Electronics for the ATLAS New Small Wheel Project*. PhD thesis, McGill University, Montreal, Canada, 2019.

[64] R. Brun and F. Rademakers. ROOT: An object oriented data analysis framework. *Nucl. Instrum. Meth. A*, 389:81–86, 1997. See also "ROOT" [software], Release 6.18/02, 23/08/2019, (https://zenodo.org/record/3895860#.YVJW6n0pCHs).

[65] Fabio Sauli. Principles of operation of multiwire proportional and drift chambers. In *Cern Yellow Reports: Monographs*, page 92 p, Geneva, 1977. CERN, CERN. CERN, Geneva, 1975 - 1976.

[66] M. Hatlo, F. James, P. Mato, L. Moneta, M. Winkler, and A. Zsenei. Developments of mathematical software libraries for the LHC experiments. *IEEE Trans. Nucl. Sci.*, 52:2818–2822, 2005.

[67] Hongwei Guo. A Simple Algorithm for Fitting a Gaussian Function [DSP Tips and Tricks]. *IEEE Signal Processing Magazine*, 28(5):134–137, September 2011.

[68] Ichita Endo, Tatsuo Kawamoto, Yoshinari Mizuno, Takashi Ohsugi, Takashi Taniguchi, and Tohru Takeshita. Systematic shifts of evaluated charge centroid for the cathode read-out multiwire proportional chamber. *Nuclear Instruments and Methods in Physics Research*, 188(1):51–58, September 1981.

[69] Bernd Stelzer. The New Small Wheel Upgrade Project of the ATLAS Experiment. *Nuclear and Particle Physics Proceedings*, 273-275:1160–1165, April 2016.

[70] Xiao Zhao, Wenlong Li, Dengfeng Zhang, Changyu Li, Han Li, Shengquan Liu, Peng Miao, Yanyan Du, Yanyun Duan, and Chengguang Zhu. Cosmic test of sTGC detector prototype made in China for ATLAS experiment upgrade. *Nuclear Instruments and Methods in Physics Research Section A: Accelerators, Spectrometers, Detectors and Associated Equipment*, 927:257–261, May 2019.

[71] Manfred Krammer. Upgrade Programs of the LHC Experiment, November 2017.

[72] Benoit Lefebvre. stgc_as_built_fit.

[73] Benoit Lefebvre. tgc_analysis.

[74] The ATLAS Collaboration. Athena.

[75] Lia Formenti. cosmics_xray_correlation.

[76] Siyuan Sun. sTGC_readout_sw.

[77] G Brianti. Large Hadron Collider in the LEP Tunnel. In *Proceedings of the ECFA-CERN Workshop*, volume 1, page 352, Lausanne and Geneva, March 1984.

[78] Letter of Intent for the Phase-I Upgrade of the ATLAS Experiment. Technical Report CERN-LHCC-2011-012. LHCC-I-020, CERN, Geneva, November 2011.

[79] ATLAS: letter of intent for a general-purpose pp experiment at the large hadron collider at CERN. Technical Report CERN-LHCC-92-004, CERN, Geneva, 1992.

[80] The ATLAS Collaboration. Technical Design Report for the Phase-I Upgrade of the ATLAS TDAQ System. Technical report, Sep 2013. Final version presented to December 2013 LHCC.

[81] Howard Georgi and S. L. Glashow. Unity of all elementary-particle forces. *Phys. Rev. Lett.*, 32:438–441, Feb 1974.

[82] Luca Lista. *Statistical Methods for Data Analysis in Particle Physics*, volume 941 of *Lecture Notes in Physics*. Springer International Publishing, Cham, 2017.

[83] K. Kodama et al. Detection and analysis of tau neutrino interactions in DONUT emulsion target. *Nucl. Instrum. Meth. A*, 493:45–66, 2002.

APPENDICES

Appendix A

Uncertainty in cluster positions

A.1 Cluster definition

A cluster is a series of contiguous strip channels on a layer with non-zero amplitude, all part of the same trigger and having the same event number [60]. Clusters result from the drift of ionization products generate in the ionization avalanche caused by a muon [55]. The peak-detector-output (PDO) of the signal on each strip of a cluster is fit with a Gaussian. The y-position of a particle as it passed through the layer is mean of the cluster, referred to here as the hit position.

A.2 Effect of fit algorithm on cluster mean

The clusters were fit with Guo's method [67] and Minuit2 for ROOT [66]. The difference in cluster means between the two algorithms is shown in figure A.1.

The RMS of the distribution in figure A.1 is 57 µm, which is much larger than the statistical uncertainty in the mean for the Minuit2 algorithm, which peaks around 7 µm. An RMS of 60 µm is common for data taken with most quadruplets at 3.1 kV. Therefore, the uncertainty in the y-hit positions is assigned 60 µm.

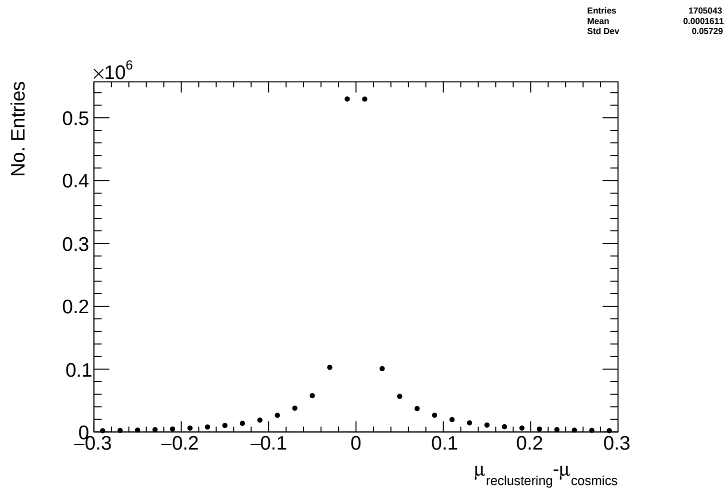

Figure A.1: The difference between cluster means calculated with Guo's method [67] in `tgc_analysis/CosmicsAnalysis` and Minuit2 for ROOT [66] in `strip_position_analysis/ReClustering` for data collected with QL2.P.8 at 3.1 kV.

A.3 Effect of uncertainty in cluster mean on track residuals

The uncertainty assigned to the hit position affected the uncertainty in the extrapolated/interpolated position of the track, and in the residuals. The bin size of the residual distributions was set to 200 µm because that was the uncertainty in the residuals calculated from the tracks with the least favourable geometry (like tracks built from hits on layers 1 and 2 and extrapolated to layer 4).

Appendix B

Study of cosmics for alignment analysis statistical uncertainty

Typically, one million triggers (cosmic muon events, noise, photons and δ-rays) were collected for each Canadian quadruplet at McGill University, resulting in roughly half the number of viable tracks after cuts. For QS3.P.18, 3.5 million triggers were collected. To gauge the sensitivity of the analysis to the available statistics, partitions of this data with each with a different number of triggers were analyzed separately. Ultimately, the quantity of interest was the gaussian mean of the residual distribution in regions of interest, so the peak in the distribution of the statistical uncertainty in the residual means for each area of interest for a specific tracking combination was used to gauge the quality of the analysis. How the peak in the residual mean uncertainty distribution changes with the number of triggers is shown in figure for tracks on layer 1 built from layers 3 and 4 B.1.

The uncertainty is already around 20 µm at 1 million triggers, suitable for distinguishing differences in offsets of order 50 µm as required. Although increased statistics could decrease the statistical uncertainty, it is not required for the goals of this analysis. Moreoever, the systematic uncertainty is around 50 µm and the systematic uncertainty on the x-ray residuals is 150 µm so the statistical uncertainty of 20 µm is nearly negligible.

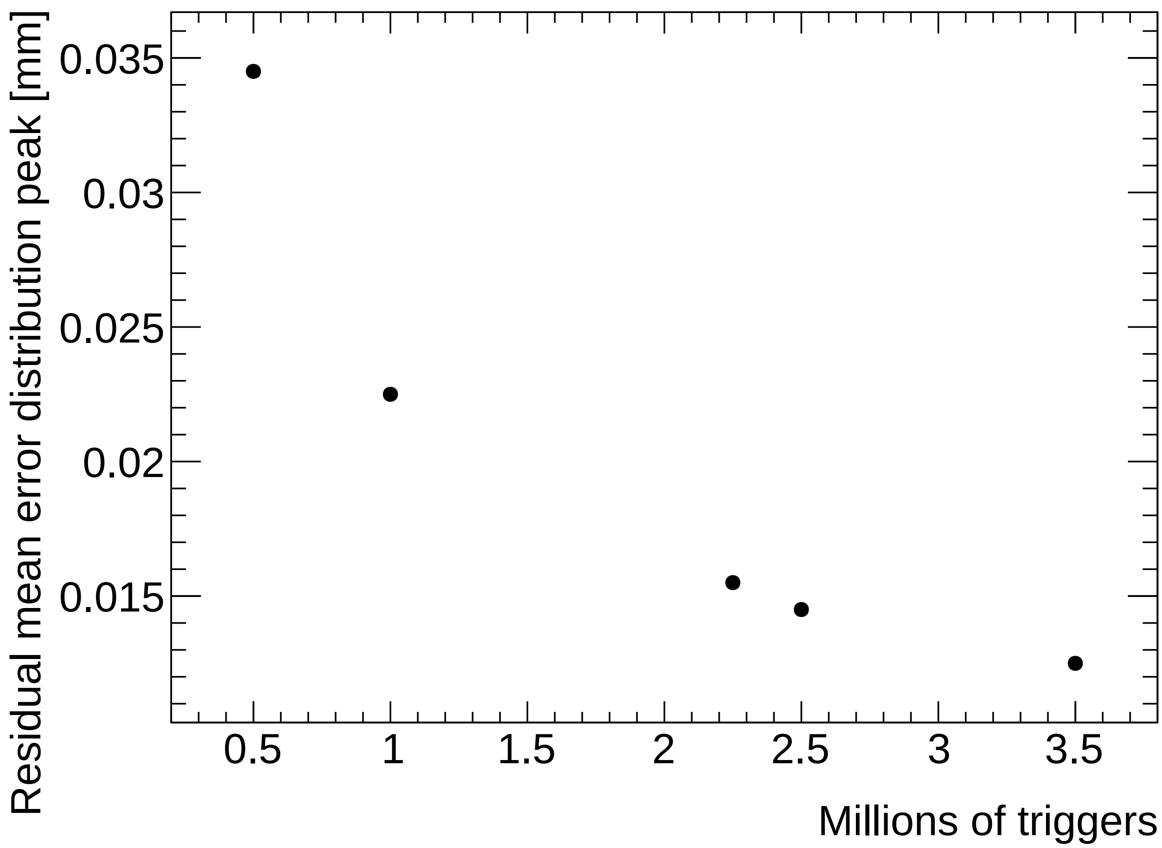

Figure B.1: How the peak of the distributions of uncertainties in the residual means in regions ofinterest for tracks on layer 1 built from layers 3 and 4 changed with the number of triggers used in the analysis. The distribution falls off as $\frac{1}{\sqrt{N}}$ as expected.

Appendix C

Study of systematic uncertainties when using cosmics data for alignment studies

C.1 Residual distribution fit function

The distribution of residuals should be modelled by a double gaussian fit[60]:

$$G(r) = A_s exp\left[\frac{-(r-\mu)^2}{2\sigma_s^2}\right] + A_b exp\left[\frac{-(r-\mu)^2}{2\sigma_b^2}\right] \tag{C.1}$$

where r is the residual, A is the gaussian amplitude, μ is the gaussian mean, σ is the gaussian sigma, and the subscripts s and b stand for signal and background respectively. One gaussian captures the real (signal) tracks and the other captures the tracks built from noise (background). The gaussian with the smaller width is identified as the signal.

A single gaussian fit failed less often than a double gaussian fit. The gaussian fits were performed by initially estimating the amplitude to be 100 tracks, the gaussian mean to be the histogram mean, and gaussian σ to be the RMS. The fit range was restricted to ± 1 RMS from the histogram mean. The modification helped the gaussian fit capture the signal peak. An example residual distribution is shown in figure C.1.

For all residual distributions in 100 mm by 100 mm bins on layer 4 built from hits on layers 1 and 2, the difference in gaussian and double gaussian means and σ's is shown in figure C.2. Since the RMS of the residual mean differences distribution is less than 50 µm the gaussian

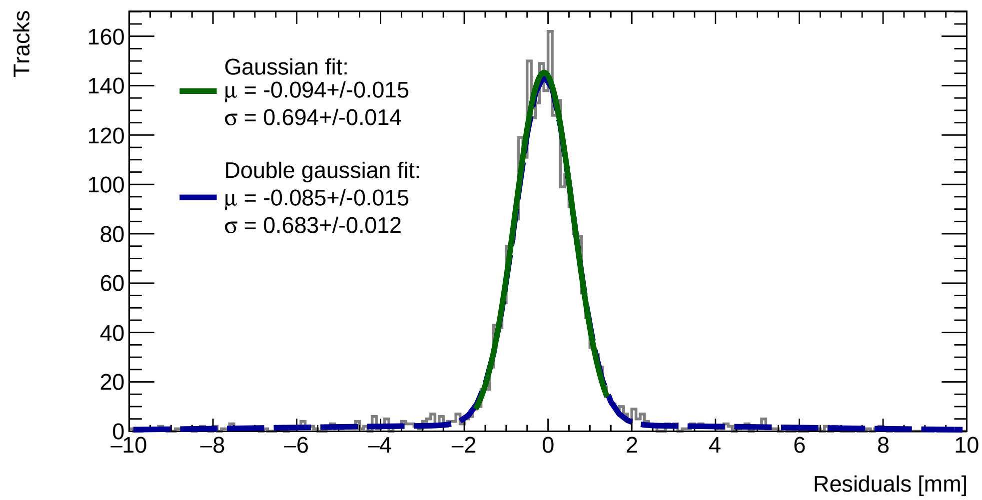

Figure C.1: Residual distribution for tracks on layer 4 built from hits on layers 1 and 2 for $x \in [-3.00, 97.00], y \in [394.60, 494.60]\, mm$ for QL2.P.8 fit with a double gaussian and a single gaussian in a range of ± 1 RMS from the histogram mean.

fit gave the same result within the required precision. Moreover, this is for the tracking combination with the worst extrapolation lever arm and the widest distribution of mean differences; the interpolation combinations have narrower distributions.

The gaussian σ should be larger than the double gaussian σ because the gaussian distribution includes the effect of the noise tracks with large residuals, while the double gaussian models signal and background residuals separately. For this analysis, only the residual mean was important, so the systematic overestimate of the signal σ in the gaussian fit shown on the right of figure C.2 was allowed.

C.2 Cosmic muon data collection voltage

Cosmic muon data was collected at 2.9 kV and 3.1 kV because although 2.9 kV is closer to the operating conditions the chambers will be subject to in ATLAS, the extra gain provided by operating at 3.1 kV increased the signal to noise ratio for pad signals. Also, the tracking efficiency was higher with data collected at 3.1 kV. The difference in gain affected the relative population of clusters of different sizes, which in turn affected the uncertainty in the strip hit positions on each layer, the uncertainty in the track positions and the residual distributions. The residual distributions for 3.1 kV data are narrower, as shown in figure C.3.

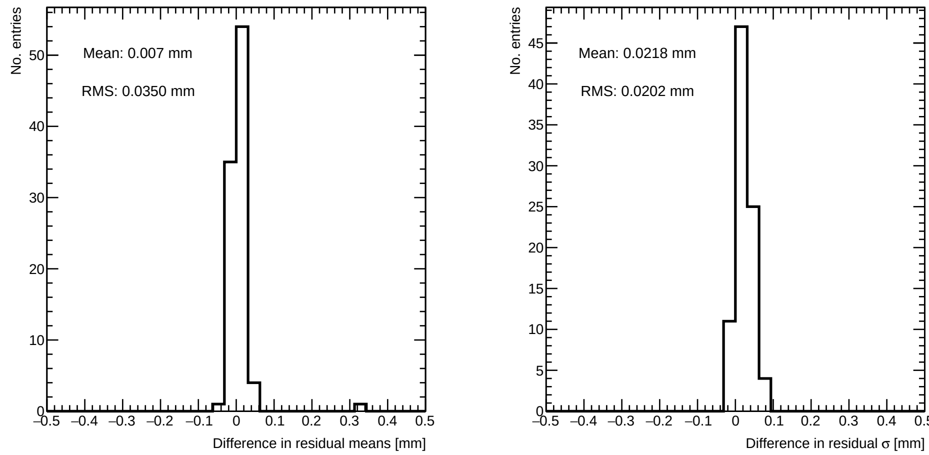

Figure C.2: Difference in residual distribution means and σ's for a gaussian and double gaussian fit, for all residual distributions in 100 mm by 100 mm bins on layer 4 built from hits on layers 1 and 2 for QL2.P.8.

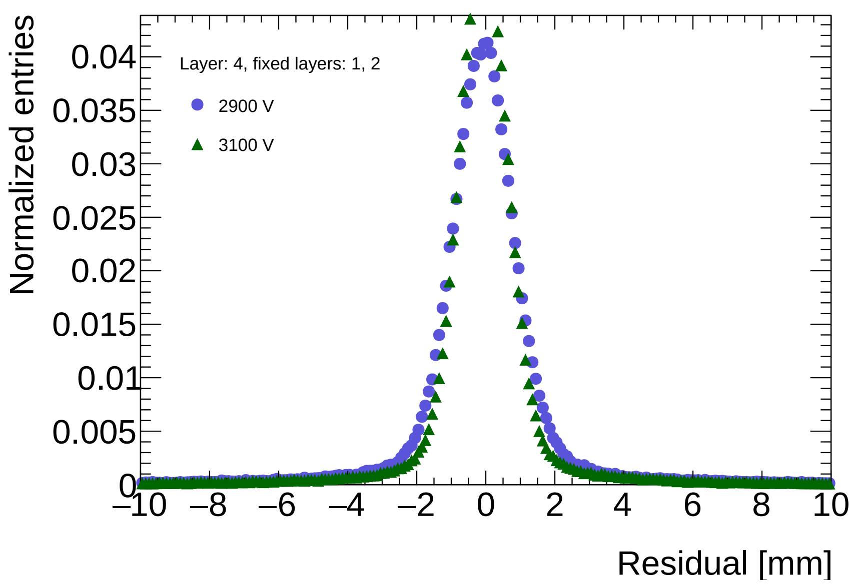

Figure C.3: Residual distribution for tracks on layer 4 built from hits on layers 1 and 2 for QL2.P.8 for data collected at 2.9 kV and 3.1 kV.

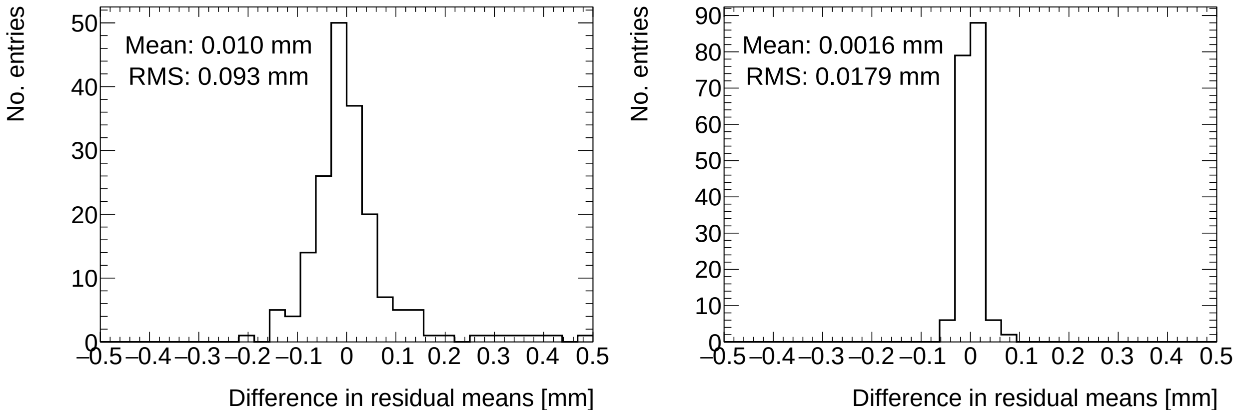

(a) Tracks on layer 4, reference layers 1 and 2. (b) Tracks on layer 2, reference layers 1 and 3.

Figure C.4: Difference in residual means for data collected with QL2.P.8 at 2.9 kV and 3.1 kV respectively in 100 mm by 100 mm bins for (a) tracks on layer 4 built from hits on layers 1 and 2 and (b) tracks on layer 2 built from hits on layers 1 and 3.

Neither dataset is better for calculating the mean of residuals in a given area, so a systematic uncertainty can be assigned based on the difference in residual means calculated for 2.9 kV and 3.1 kV data; namely, the systematic uncertainty was approximated as the RMS of the residual mean difference distribution. Data taken with QL2.P.8 was used to estimate the RMS, as in figure C.4a.

Tracks built from hits on layers 1 and 2 and extrapolated to layer 4 have the worst lever arm and hence the most uncertainty. The width of the distribution for geometrically favourable tracks are much narrower. The narrowest width of the residual mean difference distribution is for tracks on layer 2 built from hits on layers 1 and 3 (see figure C.4b).

Therefore, for each tracking combination, a systematic uncertainty equal to the RMS of the residual mean difference distribution was assigned.

C.3 Cluster fit algorithm

To ensure that changing the cluster fitting algorithm like in appendix A would not change the calculated mean of residuals in each region of interest significantly, the residual means were compared in both cases. The distribution of the difference in residual means is plotted in figure C.5 for the tracking combination with the worst extrapolation lever arm.

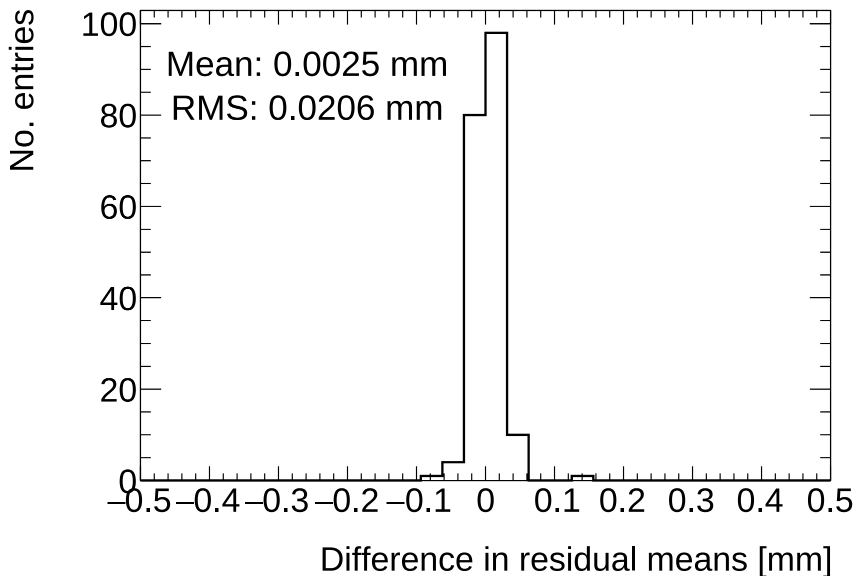

Figure C.5: Difference in residual means when the cluster fit algorithm is `Minuit2` [66] versus Guo's method [67] for tracks on layer 4 built from hits on layers 1 and 2 for QL2.P.8.

The other tracking combinations had smaller RMS values. Differences on the order of 50 µm are important, so figure C.5 shows that the clustering algorithm had a small but notable effect. Therefore, the RMS for each tracking combination will be used to add a systematic uncertainty on the residual means.

C.4 Differential non-linearity

Definition

In this context, differential non-linearity (DNL) is when the reconstructed cluster mean is biased by the fit of the discretely sampled PDO distribution over the strips. The bias depends on the relative position of the avalanche with respect to the center of the closest strip. For a summary of DNL, refer to page 40 of Lefebvre's thesis [60] and for an example application, refer to [6].

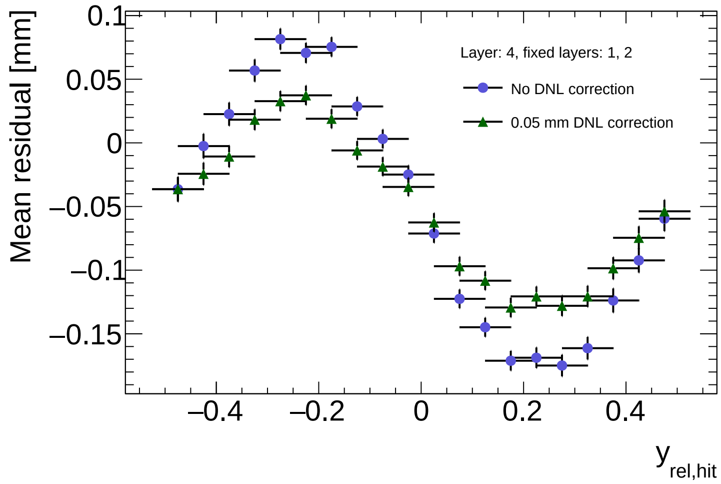

Figure C.6: Effect applying a 50 µm DNL correction to the cluster means on the residual vs y_{rel} distribution for tracks built from layers 1 and 2 and extrapolated to layer 4 for QL2.P.8.

Application and effect of DNL

The cluster mean was corrected for DNL using the equation:

$$y' = y + a\sin(2\pi y_{rel}) \tag{C.2}$$

where y is the cluster mean, y_{rel} is the relative position of the cluster mean with respect to the strip's center, a is the amplitude of the correction, and y' is the corrected cluster mean. The amplitude can be derived by comparing the reconstructed hit position to the expected hit position, as done in Abusleme, 2016 [6]. With cosmic muons, there is no reference hit position to compare to, so track residuals were used as a proxy [60]. The hallmark of the DNL effect is the periodic pattern in the residual versus y_{rel} profile, and the effect of correcting the cluster means using an amplitude of 50 µm is shown in figure C.6. An amplitude of 50 µm was based on Lefebvre's estimate of the DNL amplitudes by layer, quadruplet and cluster size using exclusive cosmic muon tracks in `tgc_analysis/CosmicsAnalysis`. Little variation was seen in the amplitude parameters with respect to the quadruplet tested, the layer and the cluster size so a universal correction was used.

Although the correction is not large enough in this case, the figure shows that the correction does reduce the DNL effect. Slightly better performance is seen in the interpolation tracking combinations where the quality of the residuals is better. DNL corrections for cosmic muon data are difficult because the DNL effect is obscured by the effect of misalignments and

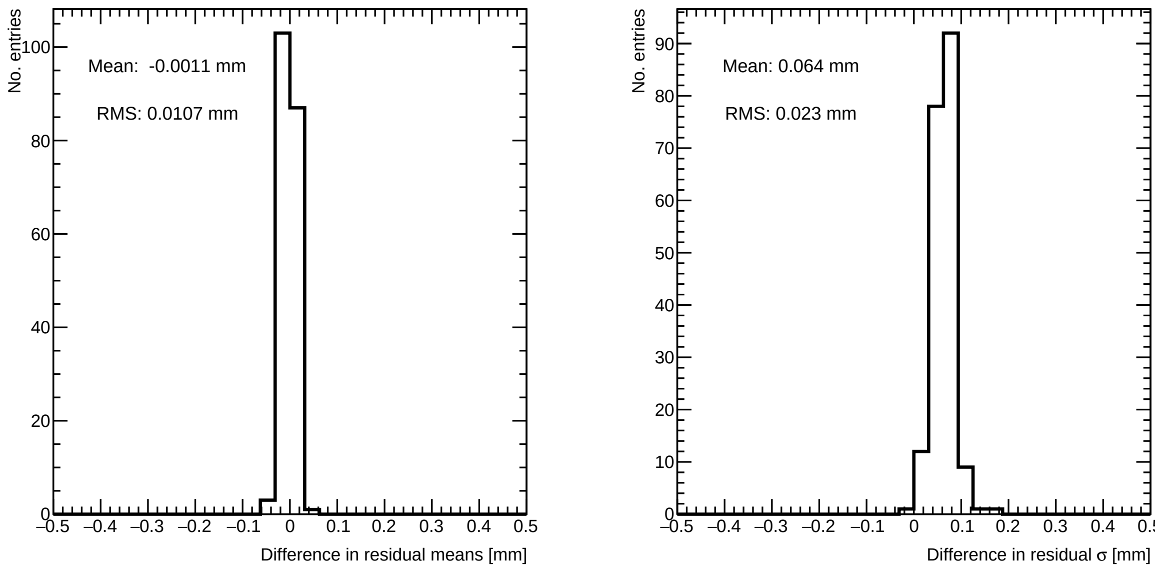

Figure C.7: Difference in residual distribution means and σ's with and without DNL correction for residuals on layer 4 from reference layers 1 and 2 for QL2.P.8.

noise. Misalignments cause the center of the sine pattern in figure C.6 to be shifted off of zero, since the mean of residuals is shifted.

In figure C.7, it is apparent that the effect of the DNL correction on the mean of the residual distribution in 100 mm by 100 mm areas is on the order of micrometers in the worst extrapolation case. Although the σ's of the residual distributions shrink with the DNL correction, the mean is the parameter of interest. Therefore, for this analysis DNL was not corrected for.

The σ's of the residual distributions do shrink with the DNL correction but not so much to affect the residual means, which are the important parameter for this analysis. Therefore, since the effect of the DNL correction is negligible, it was not pursued further.

Appendix D

Printable plots

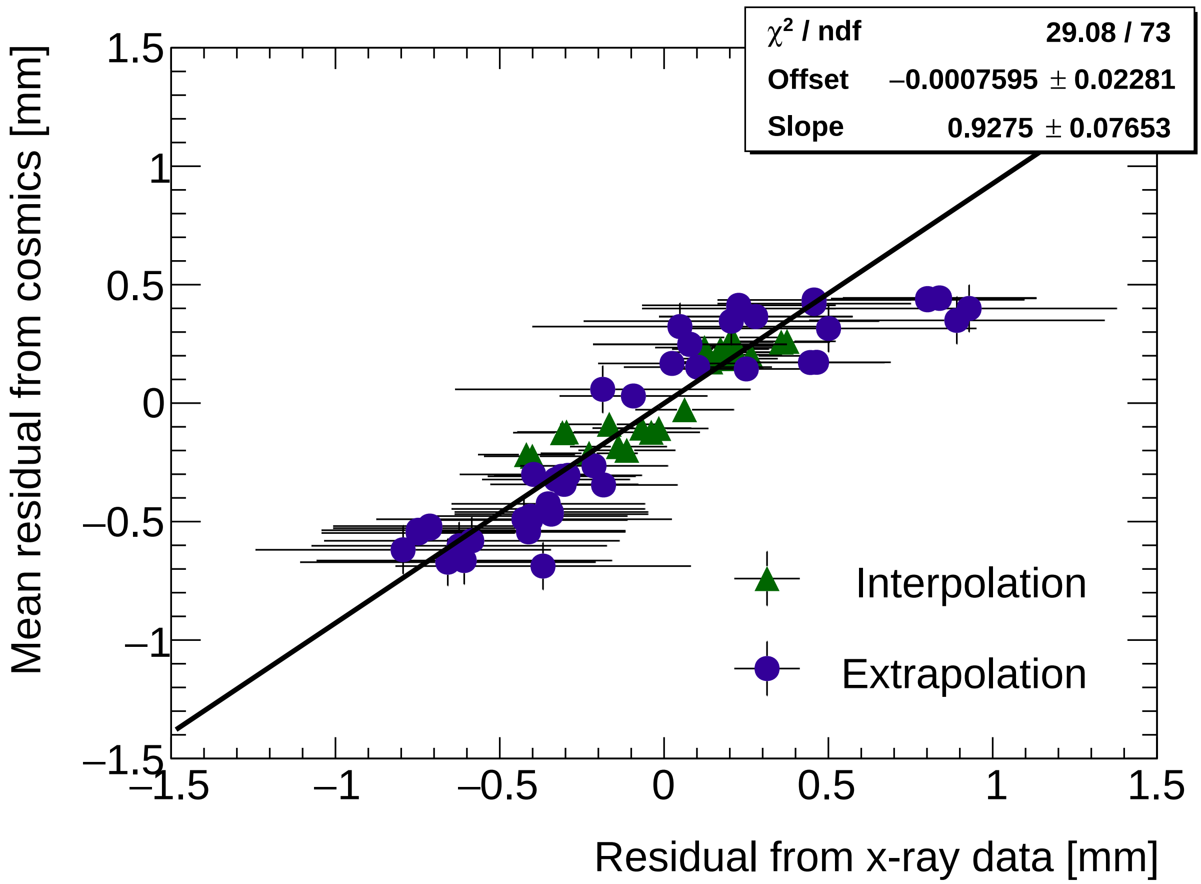

Figure D.1: Correlation plot between x-ray and cosmics residuals for all tracking combinations for QL2.P.11. Each rectangle is centered on an x-ray and mean cosmics residual pair. The width of the rectangles in x and y are the uncertainty in the x-ray and mean cosmics residual respectively. This is a printable version of figure 7.2 in section 7.1.

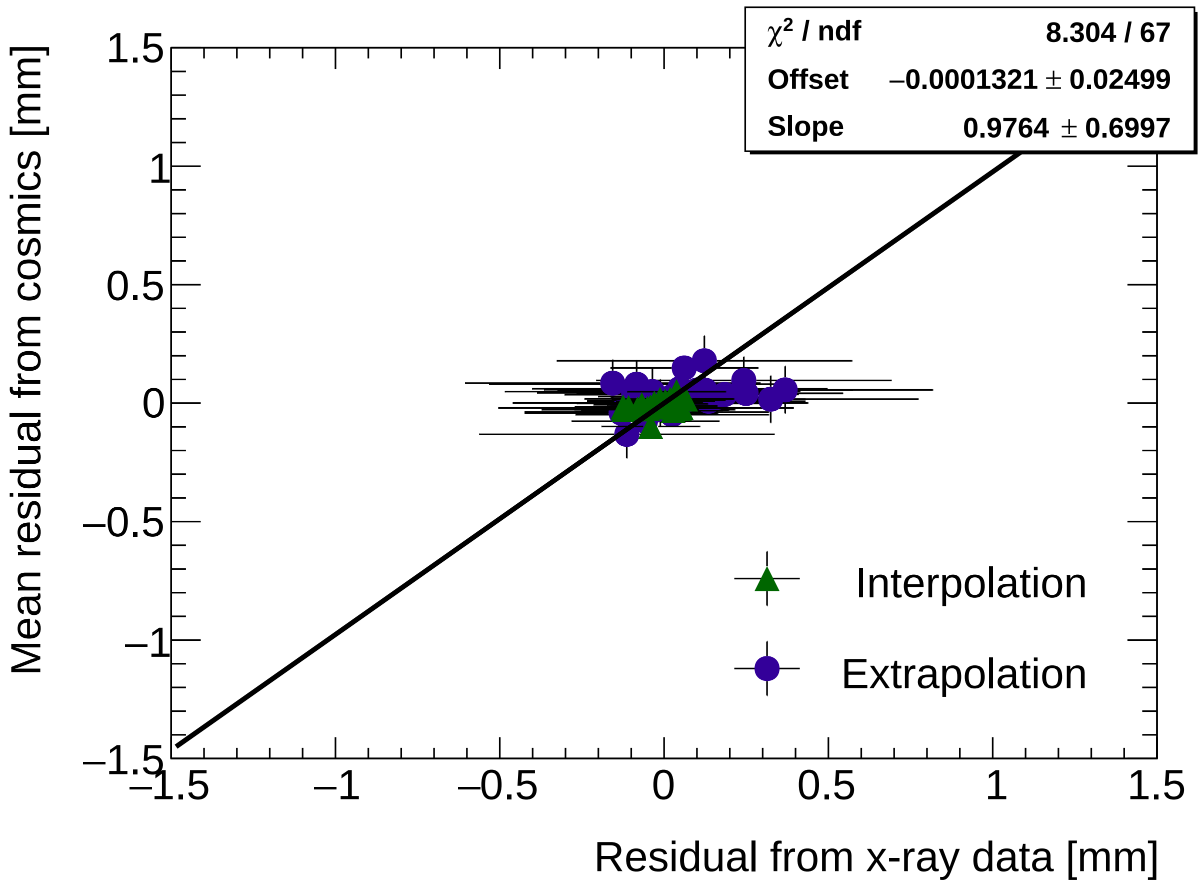

Figure D.2: Correlation plot between x-ray and cosmics residuals for all tracking combinations for QL2.P.8. Each rectangle is centered on an x-ray and mean cosmics residual pair. The width of the rectangles in x and y are the uncertainty in the x-ray and mean cosmics residual respectively. This is a printable version of figure 7.3 in section 7.1.